Cell

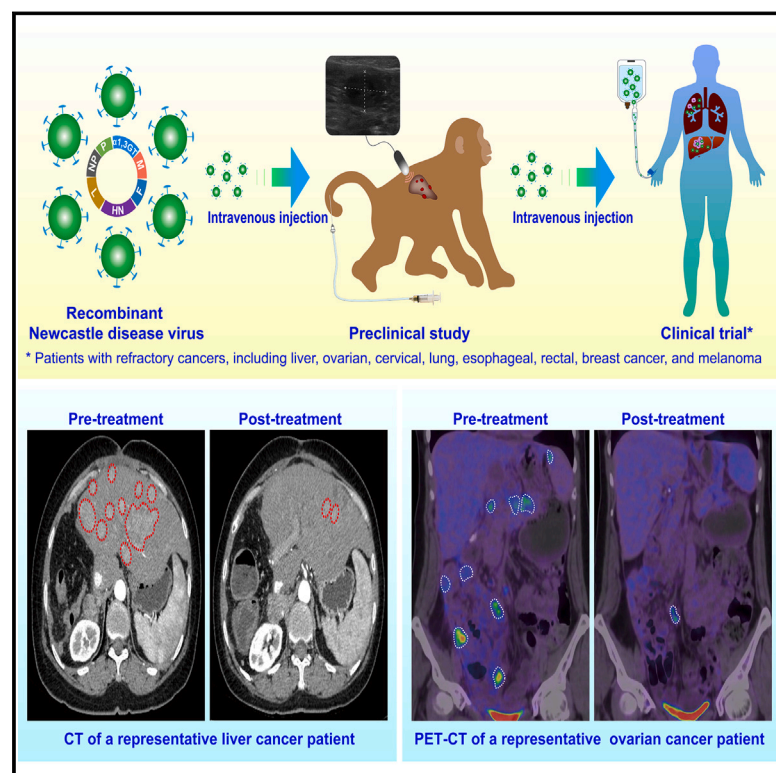# Hyperacute rejection-engineered oncolytic virus for interventional clinical trial in refractory cancer patients

Graphical abstract

Highlights

- Revolutionized oncolytic virus design using hyperacute rejection to enhance immunity

- Used CRISPR monkey liver cancer model to assess intravenous NDV-GT efficacy

- Developed a unique oncolytic virus that selectively lysed tumors safely in humans

- Employed a nonhuman primate model that improved predictions for clinical translation

Authors

Liping Zhong, Lu Gan, Bing Wang, ...,
Kun Zhang, Wei Shi, Yongxiang Zhao

Correspondence

zhongliping@gxmu.edu.cn (L.Z.),
zhang1986kun@tongji.edu.cn (K.Z.),
shiwei1001@csco.org.cn (W.S.),
zhaoyongxiang@gxmu.edu.cn (Y.Z.)

In brief

A Newcastle disease virus engineered to enhance anti-tumor immune responses provided a 90% rate of disease control in a clinical trial of 20 patients with diverse refractory cancer types and with distant metastases.

CellPress

Resource

Hyperacute rejection-engineered oncolytic virus for interventional clinical trial in refractory cancer patients

Liping Zhong,[1,13,*] Lu Gan,[1,13] Bing Wang,[2,13] Tao Wu,[3,13] Fei Yao,[4] Wenlin Gong,[1] Hongmei Peng,[3] Zhiming Deng,[3] Guoyou Xiao,[5] Xiyu Liu,[1] Jintong Na,[1] Desong Xia,[1] Xianjun Yu,[6] Zhikun Zhang,[1] Bangde Xiang,[7] Yu Huo,[1] Dan Yan,[4] Zhixin Dong,[4] Fang Fang,[4] Yun Ma,[8] Guanqiao Jin,[9] Danke Su,[9] Xiuli Liu,[1] Qiang Li,[9] Hai Liao,[9] Chao Tang,[1] Jian He,[1] Zhiping Tang,[10] Shilai Zhang,[5] Bingqing Qiu,[5] Zhi Yang,[5] Lihui Yang,[11] Ziqin Chen,[3] Mengsi Zeng,[3] Ronghua Feng,[3] Jiege Jiao,[12] Yuan Liao,[1] Tinghua Wang,[1] Liangliang Wu,[1] Zhengcheng Mi,[1] Ziqun Liu,[2] Si Shi,[6] Kun Zhang,[1,*] Wei Shi,[4,*] and Yongxiang Zhao[1,14,*]

[1]State Key Laboratory of Targeting Oncology, National Center for International Research of Biotargeting Theranostics, Guangxi Medical University, Nanning, Guangxi 530021, China
[2]Department of Spine Surgery, The Second Xiangya Hospital of Central South University, Changsha, Hunan 410011, China
[3]The First People's Hospital of Changde City, Changde, Hunan 415000, China
[4]Department of Oncology, The First Affiliated Hospital, Guangxi University of Chinese Medicine, Nanning, Guangxi 530023, China
[5]Department of Nuclear Medicine, The Affiliated Tumor Hospital, Guangxi Medical University, Nanning, Guangxi 530021, China
[6]Department of Pancreatic Surgery, The Affiliated Tumor Hospital, Fudan University, Shanghai 200032, China
[7]Department of Hepatobiliary Surgery, The Affiliated Tumor Hospital, Guangxi Medical University, Nanning, Guangxi 530021, China
[8]Department of Pathology, The Affiliated Tumor Hospital, Guangxi Medical University, Nanning, Guangxi 530021, China
[9]Department of Radiology, The Affiliated Tumor Hospital, Guangxi Medical University, Nanning, Guangxi 530021, China
[10]Department of Ultrasound, The First Affiliated Hospital of Guangxi Medical University, Nanning, Guangxi 530021, China
[11]Fundamental Nursing Teaching and Research Office, Nursing College of Guangxi Medical University, Nanning, Guangxi 530021, China
[12]Yuandan Biotechnology (Hainan) Co., Ltd., Haikou, Hainan 570100, China
[13]These authors contributed equally
[14]Lead contact
*Correspondence: zhongliping@gxmu.edu.cn (L.Z.), zhang1986kun@tongji.edu.cn (K.Z.), shiwei1001@csco.org.cn (W.S.), zhaoyongxiang@gxmu.edu.cn (Y.Z.)
https://doi.org/10.1016/j.cell.2024.12.010

SUMMARY

Recently, oncolytic virus (OV) therapy has shown great promise in treating malignancies. However, intravenous safety and inherent lack of immunity are two significant limitations in clinical practice. Herein, we successfully developed a recombinant Newcastle disease virus with porcine $\alpha 1,3GT$ gene (NDV-GT) triggering hyperacute rejection. We demonstrated its feasibility in preclinical studies. The intravenous NDV-GT showed superior ability to eradicate tumor cells in our innovative CRISPR-mediated primary hepatocellular carcinoma monkeys. Importantly, the interventional clinical trial treating 20 patients with relapsed/refractory metastatic cancer (Chinese Clinical Trial Registry of WHO, ChiCTR2000031980) showed a high rate (90.00%) of disease control and durable responses, without serious adverse events and clinically functional neutralizing antibodies, further suggesting that immunogenicity is minimal under these conditions and demonstrating the feasibility of NDV-GT for immunovirotherapy. Collectively, our results demonstrate the high safety and efficacy of intravenous NDV-GT, thus providing an innovative technology for OV therapy in oncological therapeutics and beyond.

INTRODUCTION

Oncolytic viruses (OVs), such as adenovirus, Newcastle disease virus (NDV), parvovirus, and reovirus, serve as a promising anti-tumor approach and are under investigation in pre-clinical experiments and clinical trials.[1–7] The preferential replication and oncolysis in tumor cells, along with the activated post-oncolytic immune responses, are recognized as the primary justifications for their utilization.[2,8,9] In particular, their potential in activating immune responses has been thoroughly validated and systematically explored for enhancing the anti-tumor effect.[10,11] However, the therapeutic outcomes of OVs remain unsatisfactory, primarily due to the inherent lack of immunity and insufficient propagation and spread.[8,12–14] Furthermore, the effectiveness of OVs alone in treating distant tumors is limited by the poorly stimulated and nonpersistent immune responses, as well as the exacerbated immunosuppressive microenvironment.[15–18] In this respect, various efforts have been made to attenuate antiviral

immune response,[19,20] promote the dissemination and spread of OVs,[13,21–23] ameliorate the immunosuppressive microenvironment, and bolster anti-tumor immune responses.[24–26]

Accordingly, a series of genetically engineered OVs expressing specific genes and proteins have been developed to enhance their anti-tumor effects, offering unprecedented opportunities for targeting primary and distant tumors.[13,21,22,24–26] Furthermore, therapeutic regimens combining OVs with other pharmacological treatments have progressed to clinical trial stages, with OV-augmented immunotherapy drawing significant interest.[3,27–30] However, regardless of the approach used, these trials continue to suffer from low response rates, limited clinical benefits, and reduced relevance in clinical practice.[29,31] The primary cause of the significant discrepancies between practical clinical outcomes and desired expectations can be attributed to the overestimation of these anti-tumor approaches in preclinical studies, where activated immune responses and robust oncolytic performance were observed in lower animal tumor models.

The current barriers to the clinical application of OVs can be considered through the following four points: firstly, most OVs are not efficient enough to infect and replicate in tumor cells of the human body *in vivo*.[3] Secondly, showing safety in local tumor injection, the safety of intravenous OVs remains inadequately validated.[5,6] During the rapid division and replication of existing OVs with recombinant exogenous genes, there is a risk that these exogenous genes may be deleted, leading to the loss of their traits and a potential reversion to their ancestors, thereby restoring their ability to infect and damage normal cells.[32–34] To minimize this risk, OVs must be administered locally into tumors rather than intravenously in an indirect manner. As a result, the efficacy is greatly weakened. Thirdly, the immune responses evoked by the exogenous target proteins expressed by OVs are not strong enough to overcome the immunosuppressive barrier.[35] Fourthly, OVs possess strong self-antigenicity and are prone to produce high-titer neutralizing antibodies, leading to their inability to be reused and a significant reduction in their efficacy.[1,9] We have recently developed an NDV that naturally lyses tumor cells while exhibiting weak immunogenicity. This virus neither infects nor replicates in normal cells. During the replication process of the NDV in tumors *in vivo*, no risk of damage to normal cells and tissues has been observed,[36,37] even if it reverses and reverts to the wild type.[8] Therefore, it could be an ideal OV for use in immune gene therapy.

Based on the above, our ongoing research has been dedicated to exploring the utilization of this NDV strain as a vector for delivering a specific therapeutic gene aimed at enhancing oncolytic effects. We are aware of the serious impact of the hyperacute rejection reaction triggered by the xenogeneic antigen alpha-galactosidase (αGal) on xenografts, which is a severe adverse reaction leading to xenograft failure.[38] The cardinal pathological feature of this reaction is thrombus formation caused by damage of donor vascular endothelial cells and subsequent release of platelet-activating factor (PAF). Within minutes to hours following the connection of xenografts (such as porcine hearts) to the vascular systems of recipients (human or non-human primates), a critical immunological reaction occurs.[39] The recipients harbor pre-formed natural antibodies, specifically anti-αGal, that target the xenografts. These antibodies bind to the numerous αGal epi-

topes present on the vascular endothelial cells of the xenografts. This binding initiates a destructive process, leading to cell destruction through complement-mediated cytolysis (CDC) and antibody-dependent cell-mediated cytolysis (ADCC), effectively compromising the viability of the xenografts. The damaged endothelial cells release PAF, leading to intravascular coagulation and thrombus formation, ultimately resulting in graft function loss. Anti-Gal is the most abundant naturally occurring antibody in humans.[39] Anti-Gal interacts specifically with the αGal epitope on glycolipids and glycoproteins and is produced throughout life as a result of antigenic stimulation by bacteria of the gastrointestinal flora. The αGal epitope is absent in humans because it is synthesized by the glycosylation enzyme α1,3galactosyltransferase (α1,3GT). Humans lack active α1,3GT gene due to frameshift mutations in the α1,3GT gene during evolution but produce the anti-Gal antibody in large amounts.[39] Given the unique evolution of αGal antigens and anti-αGal antibodies in mammals, this allows us to apply the hyperacute rejection theory in reverse to the field of antitumor therapy. In recent years, efforts have been made to address the challenges of low response rates and limited clinical benefits by utilizing αGal-expressing tumor cell vaccines or injecting αGal glycolipids directly into tumor.[40,41] Tumor immunotherapy based on α1,3GT gene has attracted more interest.[42,43]

In this context, we have successfully developed a recombinant NDV carrying the α1,3GT gene (NDV-GT) to effectively inhibit primary hepatocellular carcinoma (HCC) and prolong survival in cynomolgus monkeys by inducing hyperacute rejection responses. The extramembrane αGal on NDV-GT-infected tumor cells triggered hyperacute rejection and humoral and cellular immune responses while alleviating the immunosuppressive microenvironment, leading to a cascade amplification of immune effect,[44] and enabling primary liver tumor shrinkage. As an RNA virus, NDV-GT exhibits low antiviral immunity,[12,45] enabling intravenous delivery to activate systematic immune responses and facilitate metastatic tumor repression in advanced cancers. In contrast to current OVs, NDV-GT is more effective in overcoming the limitations of current OVs, such as limited intratumoral delivery, low oncolysis, and transient and weak immune responses.

Systematic experiments and mechanistic explorations were conducted on unique cynomolgus monkeys of primary HCC created using the well-established CRISPR-Cas9 technology.[46] Notably, these findings offer valuable insights for estimating the therapeutic impact of NDV-GT on HCC patients, helping to bypass the significant gap that often exists between preclinical animal models and clinical settings. The genetically modified NDV-GT has demonstrated remarkable clinical benefits in patients with advanced HCC, ovarian cancer, rectal cancer, lung cancer, breast cancer, esophageal cancer, melanoma, and cervical cancer. Our study demonstrated that NDV-GT could serve as an anti-tumor drug with significant clinical translation potential for advanced cancer patients.

RESULTS

Determination of anti-Gal antibodies (pre-existing natural antibodies) in patients and cynomolgus monkeys
Anti-Gal IgM and IgG antibodies were detected in all patients and cynomolgus monkeys. No significant difference was
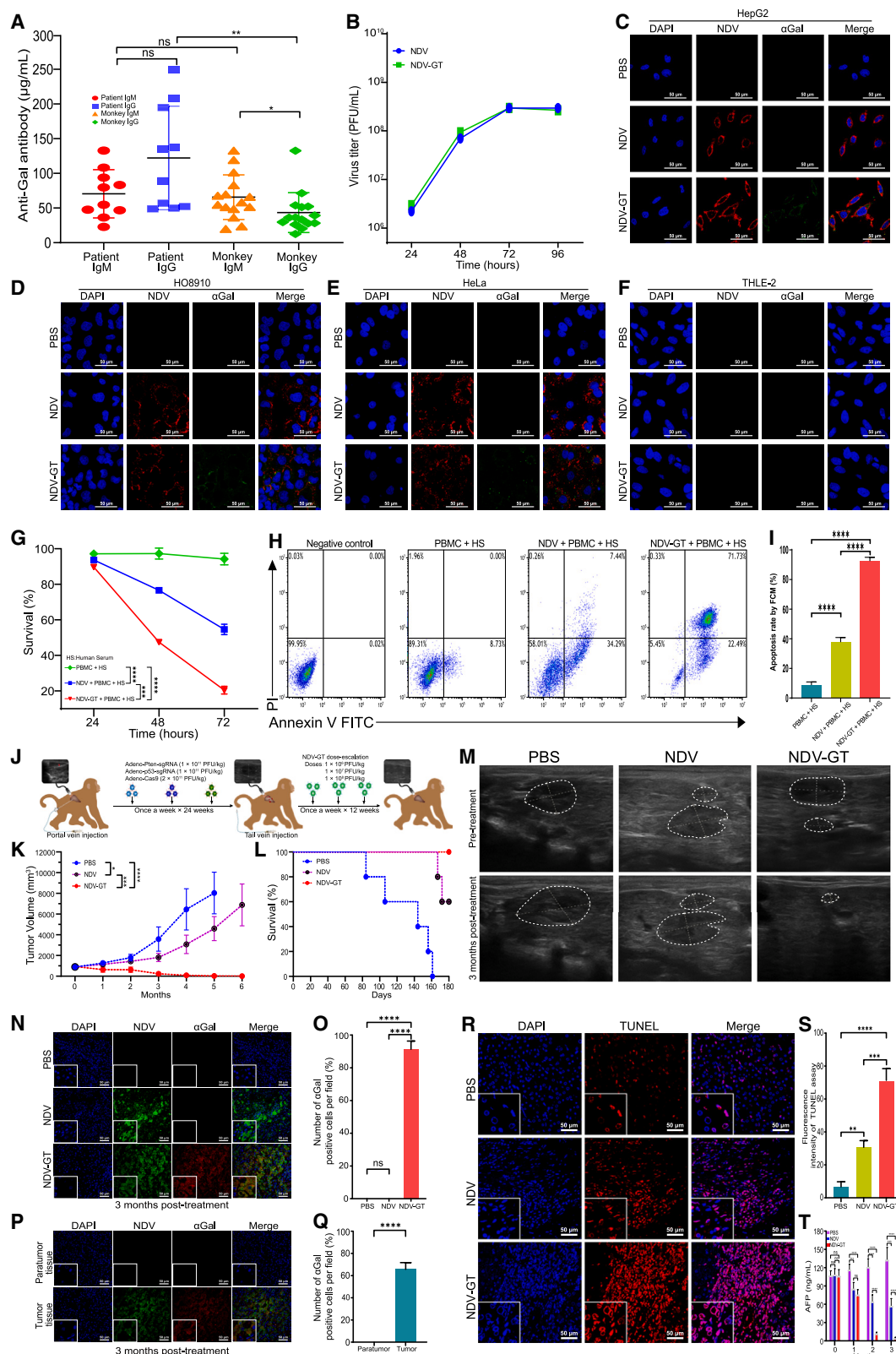
observed in the levels of anti-Gal IgM between patients and cynomolgus monkeys, while IgG levels were higher in patients than in monkeys ($p < 0.01$). There was no significant difference in anti-Gal IgG levels compared with IgM in patients ($p > 0.05$), but in cynomolgus monkeys, IgG levels were significantly lower than IgM ($p < 0.05$) (Figure 1A; Table S1).

Engineering of recombinant NDV-GT

NDV-GT was generated using a reverse genetic technique. The porcine *α1,3GT* gene was inserted into the middle of the *Pme* I enzyme cutting site within the NDV sequence (Figure S1A). The target gene segment (i.e., *α1,3GT*) was polymerase chain reaction (PCR) amplified (Figure S1B), and the successful insertion of the *α1,3GT* gene into NDV was confirmed by sequencing (Figures S1C and S1D), ensuring that the replication retention ability was maintained (Figure 1B). To investigate the specific infection, replication, and propagation of NDV-GT, we utilized HepG2 human liver cancer cells, HO8910 human ovarian cancer cells, HeLa human cervical cancer cells, and THLE-2 normal liver cells as representative models. As evidenced by the intense red and green fluorescent signals representing NDV and αGal, respectively, the parental NDV and recombinant NDV-GT successfully infected HepG2, HO8910, and HeLa cells. Additionally, the exogenous *α1,3GT* gene was efficiently expressed in the tumor cells (Figures 1C–1E). By contrast, no fluorescence signal of the αGal was observed in immortalized human liver cells (THLE-2) normal cells treated with NDV and NDV-GT, suggesting minimal infection and invasion of OVs in these cells (Figure 1F). Similar findings were observed in other tumor cells, including A549 human lung adenocarcinoma cells, TE-10 human esophageal squamous cell carcinoma cells, SK-MEL-28 human mela-noma cells, MDA-MB-231 human breast cancer cells, LS513 human colon adenocarcinoma cells, and normal cells, including human umbilical vein endothelial cells (HUVECs), IMR-90 human lung fibroblast cells, H9C2 embryonic rat heart cells, HEK293T human embryonic kidney cells, H9 human embryonic stem cells, sperm, ovum, and blastula (Figures S2A–S2M). These findings suggested the specific targeting of NDV-GT to tumor cells. Furthermore, the recombinant NDV-GT demonstrated superior inhibitory effects on HepG2 proliferation compared with parental NDV (Figure 1G). The augmented lysis ability conferred by αGal allowed NDV-GT to induce the highest level of apoptosis in HepG2 cells (Figures 1H and 1I). These suggested that the expression of the αGal enhanced the oncolytic potency of NDV-GT. Incubation for 72 h resulted in an inhibition rate of approximately 90%. Similar findings were observed in other tumor cells, including HO8910, HeLa, A549, and TE-10 (Figures S3C–S3H). These results highlighted the potential of NDV-GT as a therapeutic agent for tumor treatment.

NDV-GT's oncolytic effect and elucidating its underlying mechanisms in cynomolgus monkeys with CRISPR-mediated primary liver cancer

The use of HCC cynomolgus monkey model can facilitate the translation of NDV-GT from fundamental research to clinical application due to its high homology with humans. We injected the CRISPR-Cas9 into the liver of cynomolgus monkeys through the intrahepatic portal vein under color-ultrasound guidance, inducing efficient loss-of-function mutations of *Pten* and *p53* genes to rapidly model a primary liver tumor. Subsequently, we employed the HCC cynomolgus monkey model to investigate the *in vivo* anti-tumor effects of NDV-GT (Figure 1J). Following

---

Figure 1. Analysis of pre-existing anti-Gal antibodies in patients and primary HCC monkeys and engineering and preclinical validation of NDV-GT

(A) The mean levels of anti-Gal IgM and IgG (natural antibodies) in representative patients and cynomolgus monkeys were determined by enzyme-linked immunosorbent assay (ELISA). Data are expressed as mean ± standard deviation (SD) (patients: $n = 10$; monkeys: $n = 15$), and ns: no significance, *$p < 0.05$, and **$p < 0.01$.

(B) NDV-GT replication kinetics curve. Representative titer measurements at 24, 48, 72, and 96 h post-infection in BHK-21 cells infected with NDV-GT.

(C–F) Laser confocal scanning microscopy (LCSM) images of HepG2 (C), HO8910 (D), HeLa (E), and THLE-2 (F) cells following infection with NDV or NDV-GT for 1 h. Blue, red, and green fluorescence represent nuclei, NDV infection/replication, and αGal expression, respectively. Scale bars, 50 μm. 1,000× for the views.

(G) Viability of HepG2 cells was measured by CCK-8 assay after incubation with PBMC + HS, NDV + PBMC + HS, or NDV-GT + PBMC + HS for 24, 48, and 72 h. HS, human serum. Data are expressed as mean ± SD ($n = 6$), ***$p < 0.001$, and ****$p < 0.0001$. See also Figures S3H–S3L.

(H and I) Flow cytometry (FCM) profiles (H) and quantitative data (I) of HepG2 cells 72 h after incubation with PBMC + HS, NDV + PBMC + HS, or NDV-GT + PBMC + HS. Data are expressed as mean ± SD ($n = 6$), ****$p < 0.0001$. See also Figures S3C–S3G.

(J) Schematic diagram illustrating the process of modeling primary HCC in monkeys and the NDV-GT treatment protocol.

(K and L) Tumor growth profiles and survival rates of primary HCC cynomolgus monkeys with different treatments. Data are expressed as mean ± SD ($n = 5$), *$p < 0.05$, ***$p < 0.001$, and ****$p < 0.0001$.

(M) Representative color-ultrasound images of cynomolgus monkeys with primary HCC before and after different treatments for 3 months following which HCC disappeared (white circles indicate tumor lesions).
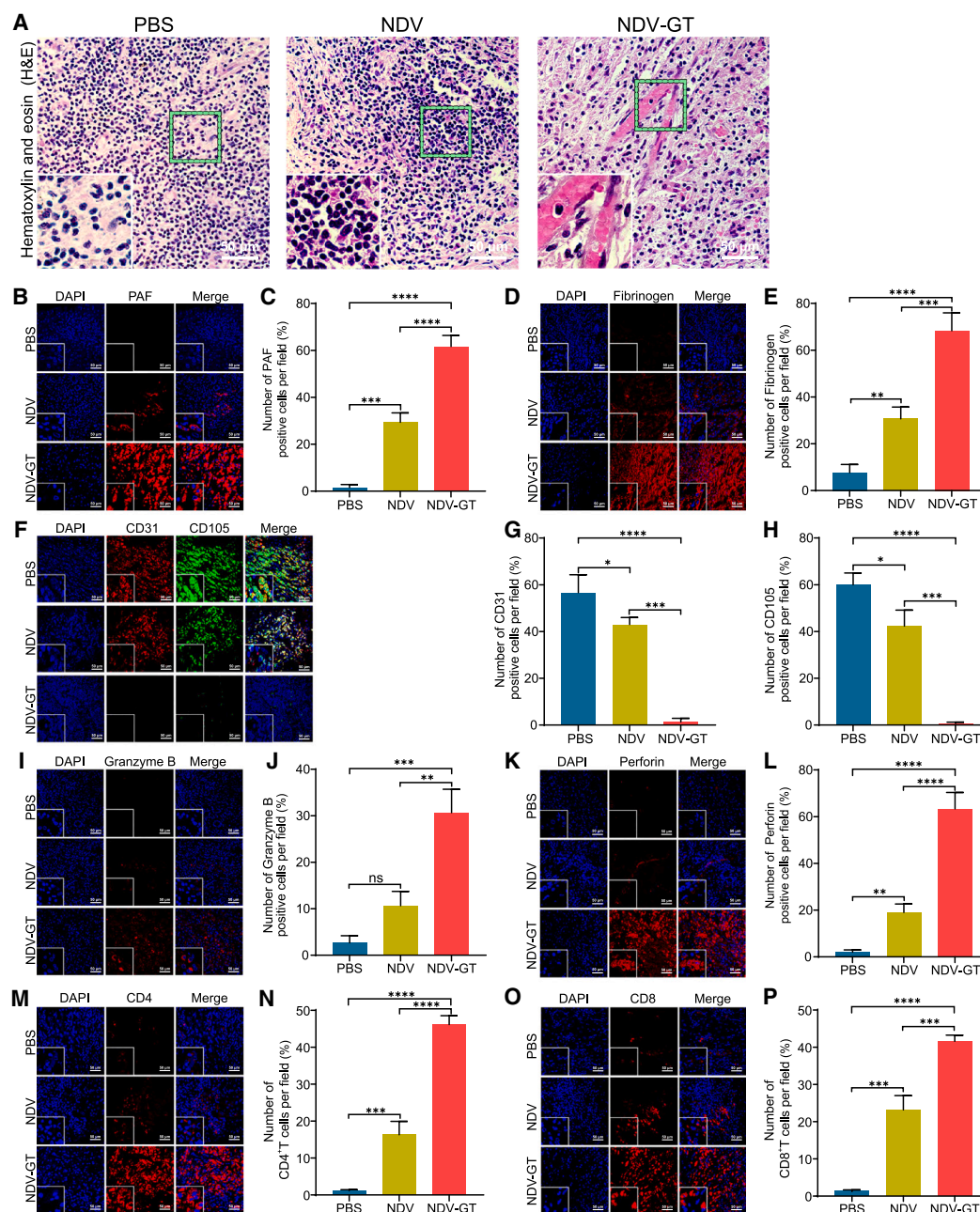
(N and O) Immunofluorescence LCSM images (N) and quantitative data (O) of αGal expression in HCC tissues with different treatments, wherein αGal expression, represented by red fluorescence, was only observed in the NDV-GT treatment group. Scale bars, 50 μm. 400× and 1,000× for the small box. Data are expressed as mean ± SD ($n = 3$), and ns: no significance, and ****$p < 0.0001$.

(P and Q) LCSM images (P) and quantitative data (Q) of αGal expression in both tumor and paratumor tissues, wherein αGal expression was only observed in the tumor tissues treated with NDV-GT, and no expression was detected in the paratumor tissues. Scale bars, 50 μm. 400× and 1,000× for the small box. Data are expressed as mean ± SD ($n = 3$), and ****$p < 0.0001$.

(R and S) TUNEL immunofluorescence images (R) and quantitative data (S) of HCC slices harvested from cynomolgus monkeys with primary HCC following treatment with PBS, NDV, or NDV-GT are presented for the detection of cell apoptosis, as indicated by the presence of red fluorescence. Scale bars, 50 μm. 400× and 1,000× for the small box. Data are expressed as mean ± SD ($n = 3$), **$p < 0.01$, ***$p < 0.001$, and ****$p < 0.0001$.

(T) Levels of AFP tumor marker in the blood of monkeys with HCC at different treatment time points (0, 1, 2, and 3 months). Data are expressed as mean ± SD ($n = 5$), and ns: no significance, ***$p < 0.001$, and ****$p < 0.0001$.

See also Figures S1, S2, and S7 and Tables S1 and S2.

Figure 2. H&E staining and immunofluorescence imaging of HCC tumors in cynomolgus monkeys: Expression of PAF, fibrinogen, CD31, CD105, granzyme B, perforin, and infiltration of CD4+ and CD8+ T cells

(A) H&E staining images of HCC slices harvested from HCC monkeys following different treatments, revealing extensive thrombosis and necrosis in the NDV-GT treatment group. Scale bars, 50 μm. 400× and 1,000× for the small box.

(B–E) LCSM images (B and D) and corresponding quantitative data (C and E) of PAF (B and C) and fibrinogen (D and E) expression were collected from HCC tissue sections harvested from cynomolgus monkeys in various treatment groups with primary HCC. Scale bars, 50 μm. 400× and 1,000× for the small box. Data are expressed as mean ± SD ($n = 3$), **$p < 0.01$, ***$p < 0.001$, and ****$p < 0.0001$.

(F–H) LCSM images (F) and quantitative data (G and H) of two vascular markers, CD31 and CD105, in tumor slices harvested from the cynomolgus monkeys with primary HCC after different treatments. CD31 and CD105, visualized by immunofluorescence staining as red and green fluorescence, respectively, exhibit significantly reduced expression in the NDV-GT group. The lowest levels of CD31 and CD105, along with the highest PAF expression, suggested thrombus formation in the tumor undergoing starvation treatment. Scale bars, 50 μm. 400× and 1,000× for the small box. Data are expressed as mean ± SD ($n = 3$), *$p < 0.05$, ***$p < 0.001$, and ****$p < 0.0001$.

(legend continued on next page)

the intravenous injection of NDV-GT, tumor tissues were surgically biopsied at 0, 24, 48, 72, and 96 h, stained for immunofluorescence, and analyzed to investigate the timing and extent of NDV-GT spread in monkey liver tumors. The results showed that the number of green fluorescent cells, representing NDV, progressively increased over time, peaking at 72 h and remaining widespread at 96 h (Figure S2N). At the end of the third month post-treatment, tumors in the NDV-GT group were significantly smaller than those in both the NDV group and PBS group (Figure 1K; Table S2). Notably, the tumors completely disappeared 3 months after treatment cessation, and as of the submission of the manuscript, all the monkeys in this group remain alive (Figure 1L; Table S2). While tumor growth was significantly delayed in the NDV group compared with the PBS group, tumors rebounded rapidly after treatment cessation, leading to the demise of two monkeys at 3 months post-treatment. In the PBS group, the longest survival time exceeded 5 months, the shortest was around 3 months, and the average survival was just over 4 months. Color-ultrasound imaging revealed tumor regression and even disappearance in monkeys treated with NDV-GT (Figure 1M). αGal was solely observed in tumor tissues treated with NDV-GT and not in paratumor tissues (Figures 1N–1Q; Table S2). αGal was exclusively detected in NDV-GT-treated liver cancer tissues, absent in paratumor tissues (1.0–1.5 cm from the margin), distinguished by alpha fetoprotein (AFP) and αGal markers (Figures 1N–1Q; Table S2). TUNEL analysis revealed the induction of extensive cell apoptosis by NDV-GT (Figures 1R and 1S; Table S2), leading to tumor regression along with a significant reduction in AFP, a marker of HCC (Figure 1T; Table S2).

Thrombi formation within the tumor blocked blood vessels (Figure 2A). We observed a significant increase in the expression levels of PAF (Figures 2B and 2C; Table S2) and fibrinogen (Figures 2D and 2E; Table S2) in tumor tissues following NDV-GT treatment, accompanied by signs of thrombus formation. The significantly reduced expression of tumor neovascular endothelial cell markers (CD31 and CD105) post-NDV-GT treatment suggested that the thrombi were primarily due to vascular atrophy and occlusion within the tumor (Figures 2F–2H; Table S2). Such findings implied that NDV-GT treatment effectively expressed αGal, which became the target of natural antibodies within tumor blood vessels. This targeting interaction triggered hyperacute rejection, leading to platelet activation and aggregation. These processes collectively facilitated the formation of thrombi and vascular occlusion, ultimately resulting in tumor shrinkage and necrosis. Furthermore, the hyperacute rejection triggered the activation and subsequent amplification of both humoral and cellular immune responses, ultimately leading to complete tumor regression in the NDV-GT-treated group.

Using immunofluorescence staining, we detected the deposition of activated complement C3b and C4b in tumor tissue sections of NDV-GT-treated cynomolgus monkeys with HCC (Figure S3A). The results showed significant deposition of activated complement C3b and C4b in the liver tissues of the NDV-GT treatment group, while none was observed in the control group, suggesting the involvement of complement activation in hyperacute rejection. Based on the above, we performed an *in vitro* NDV-GT killing experiment under conditions simulating the *in vivo* human environment, evaluating the antigen-antibody-mediated immune response and complement activation using immunofluorescence staining. This analysis revealed the deposition of activated complement components C3b and C4b on tumor cells. After blocking αGal with an anti-αGal antibody in NDV-GT-treated cells, a significant reduction in complement deposition was observed, indicating that complement activation was antibody-dependent (Figure S3B). To further investigate, we pre-blocked the αGal antigen with the same antibody and assessed NDV-GT's cytotoxic effects on various tumor cells using the cell counting kit-8 (CCK-8) assay and flow cytometry (Figures S3C–S3L). The results demonstrated that blocking αGal markedly reduced the killing effect of NDV-GT, whereas NDV's cytotoxicity remained unaffected, emphasizing the critical role of natural antibodies in complement-mediated cytotoxicity. In summary, the complement system was activated through the interaction between αGal antigen and anti-αGal natural antibody, thereby triggering hyperacute rejection. This discovery further supported our conclusions.[47–49]

The expressions of granzyme B (Figures 2I and 2J; Table S2) and perforin (Figures 2K and 2L; Table S2) were significantly elevated in NDV-GT-infected tumor tissues compared with the NDV or PBS groups, indicating xenoantigen-triggered anti-tumor immune reactions that recruited and facilitated the infiltration of CD4^{+} and CD8^{+} T lymphocytes (Figures 2M–2P; Table S2).[50,51] Specifically, NDV-GT infection of tumor cells induced αGal expression, which bound to natural anti-αGal antibodies, triggering ADCC and tumor cell destruction, while NDV-GT also directly lysed tumor cells. This process released αGal and tumor antigens, activating adaptive immunity via antigen-presenting cells. Moreover, inflammation and chemokines in the tumor microenvironment promoted T cell migration and infiltration, emphasizing the importance of CD4^{+} and CD8^{+} T cell activation for successful immunotherapy. αGal, as a natural antigen, promoted T cell differentiation, proliferation, and activation, leading to the secretion of interferon (IFN)-γ and tumor necrosis factor alpha (TNF-α) by CD4^{+} and CD8^{+} T cells.[44,52] Consequently, NDV-GT infection not only exerted direct oncolytic effects but also induced high αGal expression, potentially eliciting hyperacute rejection and initiating immune responses that suppressed tumor growth.

It is critical to understand the molecular mechanisms behind NDV-GT's oncolytic effect. Employing chip technology, we

(I–L) LCSM images (I and K) and quantitative data (J and L) of granzyme B (I and J), and perforin (K and L) expression in harvested monkey HCC slices from different treatment groups, showing the highest expression in the NDV-GT group. Scale bars, 50 μm. 400× and 1,000× for the small box. Data are expressed as mean ± SD (n = 3), and ns: no significance, **p < 0.01, ***p < 0.001, and ****p < 0.0001.

(M–P) LCSM images (M and O) and quantitative data (N and P) of CD4^{+} (M and N) and CD8^{+} T cells (O and P) in tumor slices harvested from the cynomolgus monkeys with primary HCC from different treatment groups. The highest CD4^{+} and CD8^{+} T cells infiltration is represented by red fluorescence. Scale bars, 50 μm. 400× and 1,000× for the small box. Data are expressed as mean ± SD (n = 3), ***p < 0.001, and ****p < 0.0001.

See also Figures S3 and S7 and Table S2.

A through **H** figure panels.
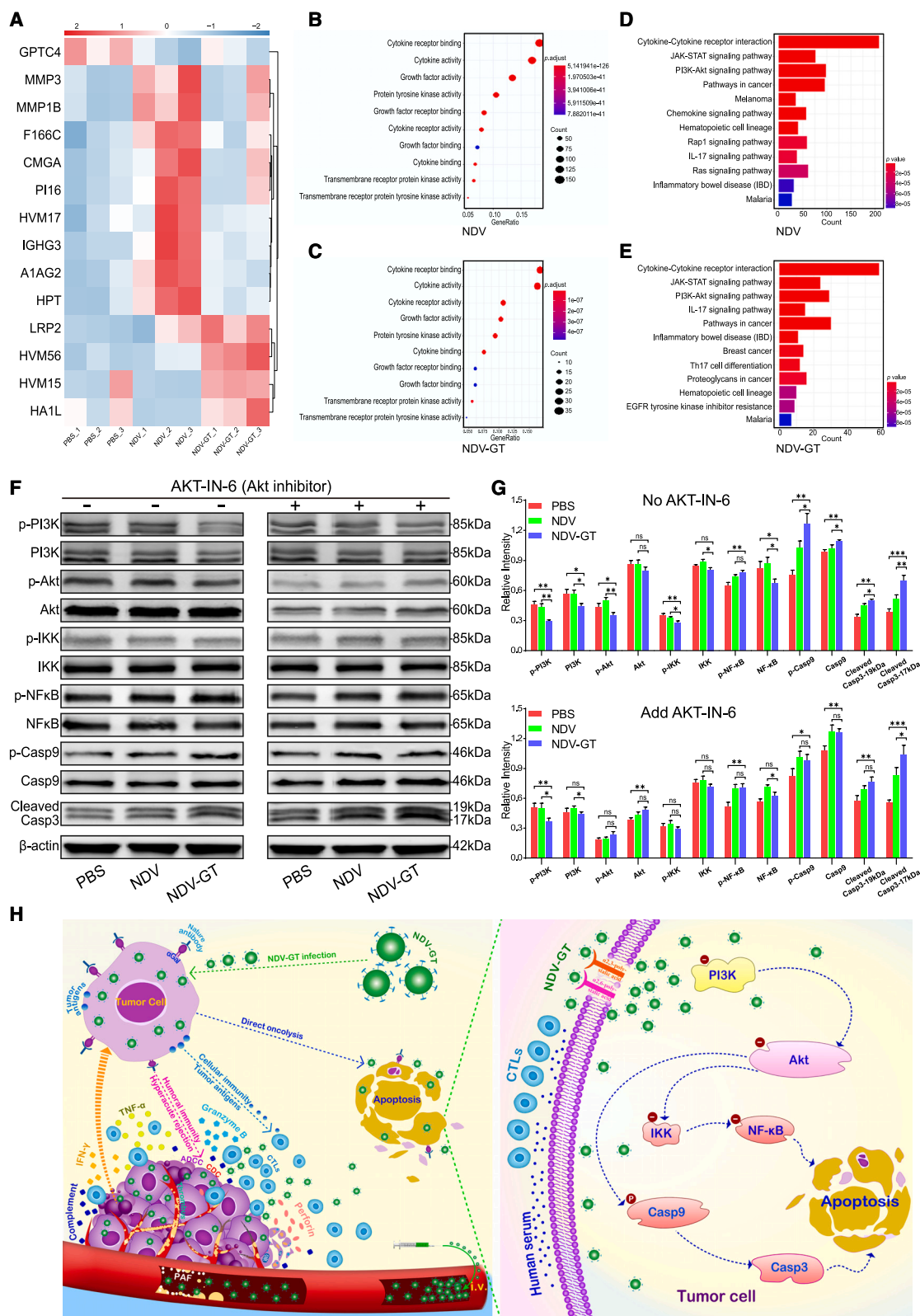
identified post-treatment differentially expressed proteins, with tandem mass tag analysis revealing apoptosis-related alterations, notably low-density lipoprotein receptor-related protein 2 (LRP2), and minimal cytokine/receptor variations in NDV-infected HepG2 cells (Figures 3A–3C). Proteins in Janus kinase-signal transducer and activator of transcription (JAK-STAT), phosphatidylinositol 3-kinase (PI3K)-protein kinase B (Akt), Ras, and interleukin (IL)-17 pathways, especially Akt, showed differential expression. Enriched factor analysis emphasized Akt-IκB kinase (IKK)-nuclear factor κB (NF-κB) signaling enrichment (Figures 3D and 3E), suggesting NDV-GT's impact on apoptosis. Western blotting following Akt inhibitor (AKT-IN-6) treatment validated NDV-GT's downregulation of Akt, IKK, and NF-κB phosphorylation while also upregulating caspase-9 and cleaved caspase-3 (Figure 3F), confirming its apoptosis induction via Akt-IKK-NF-κB inhibition (Figure 3G; Table S3).[53,54] Thus, NDV-GT effectively mediated apoptosis via Akt-IKK-NF-κB pathway (Figure 3H), novel insight into liver cancer therapy despite limited analysis.

NDV-GT could directly lyse tumor cells, destroy intratumoral blood vessels, and encode αGal, leading to hyperacute rejection and thrombus formation. Subsequently, NDV-GT alleviated the immunosuppressive microenvironment and activated humoral and cellular immunity, easing infiltration barriers, recruiting T cells, and amplifying cascade immune responses.

Safety evaluation of NDV-GT in cynomolgus monkeys

The NDV-GT treatment did not affect the body weights, body temperatures, and heart rates of the cynomolgus monkeys and had negligible effects on their physiological indices, coagulation factors, liver and kidney functions, and blood glucose levels (Table S2). Furthermore, there were no changes in urinary protein, white blood cells, and fecal occult blood (Table S2), and there was no observable damage to the normal organs of the monkeys (Figure S7A). Cynomolgus monkeys were administered intravenous NDV-GT once weekly for 12 weeks. The neutralizing

antibody titers of NDV were assessed 1 day prior to treatment initiation, as well as 1, 2, 4, 6, 8, and 12 weeks post-injection and 4 weeks post-treatment cessation. The titer of anti-NDV neutralizing antibody in the blood of the cynomolgus monkeys was observed to increase slightly but remained within the normal control value range and was clinically insignificant (Table S2). Notably, the production of neutralizing antibodies did not negatively impact the therapeutic efficacy of this OV.

Application of NDV-GT in treating 23 patients with refractory cancers (liver, ovarian, cervical, lung, esophageal, rectal, and breast) and melanoma

The established biosafety and oncolytic mechanisms in the HCC cynomolgus monkey model provided a strong foundation for expanding NDV-GT treatment in cancer patients. Within this context, an interventional clinical trial (ChiCTR2000031980) enrolled 23 patients with refractory cancers, including advanced HCC (patients P1, P12, and P19), ovarian cancer (P2, P3, P16, P17, P21, and P22), rectal cancer (P4, P18 [withdrew from clinical study after 5 weeks of treatment because of the COVID-19 pandemic], and P23 [withdrew from clinical study after 7 weeks of treatment because of the COVID-19 pandemic]), lung cancer (P5 [withdrew from clinical study after 5 weeks of treatment because of the COVID-19 pandemic], P6, and P7), breast cancer (P8 and P9), esophageal cancer (P10), melanoma (P11), and cervical cancer (P13–P15 and P20). The comprehensive patient details are displayed in Figure 4A and Table S4, including immunemodified response evaluation criteria in solid tumors (imRECIST) criteria for assessing responses in solid tumors: complete remission (CR), partial remission (PR), stable disease (SD), and progressive disease (PD).[55] The majority of these patients demonstrated a disease control rate (DCR) of 90.00% (DCR% = (CR (1 case) + PR (6 cases) + SD (11 cases))/(CR (1 case) + PR (6 cases) + SD (11 cases) + PD (2 cases)) × 100% = (18 cases/20 cases) × 100% = 90.00%) to NDV-GT treatment without significant toxicity (Figures 4B and 4C; Table S4). These preliminary results further

---

Figure 3. NDV-GT directly dissolved tumors and activated the immune cascade against cancer

(A) Heatmap, a visual representation of protein expression differences in tumor tissues from HCC-bearing monkeys infected with NDV and NDV-GT in the different treatment groups.

(B and C) Bubble charts showing differential protein expression in HCC-monkey tumors, treated with NDV (B) and NDV-GT (C). The analysis involves differential protein Gene Ontology (GO) enrichment. The x axis denotes the gene ratio, with larger bubbles indicating a higher number of genes enriched in the signaling pathway. The color transition from blue to red indicates a gradual decrease in the p values.

(D and E) Kyoto Encyclopedia of Genes and Genomes (KEGG) pathway enrichment analysis of differentially expressed proteins in HCC-monkey tumor tissues treated with NDV (D) and NDV-GT (E). The x axis displays the number of proteins enriched in the respective signaling pathway, while the color transition from blue to red indicates a descending order of p values.

(F) Western blotting demonstrated altered expression levels of proteins involved in oncolytic tumorigenesis in HepG2 cells, following treatment with the AKT-IN-6 inhibitor targeting key molecules in the signaling pathway.

(G) Relative quantitative data of various proteins derived from the analysis presented in (F). Data are presented as the mean ± SD (n = 3), and ns: no significance, *p < 0.05, **p < 0.01, and ***p < 0.001.

(H) Molecular immune profile of NDV-GT in lysis of tumors. This entire process was a coordinated effort between.

NDV-GT and the immune system to effectively eliminate the tumor. At the immunological level, when administered to cynomolgus monkeys with liver cancer, NDV-GT directly lysed tumor cells, releasing both known and previously unknown tumor antigens during this process that activated peripheral blood mononuclear cells (PBMCs) into cytotoxic T lymphocytes (CTLs). These CTLs secreted cytokines, including IFN-γ, TNF-α, granzyme B, and perforin, crucial for tumor destruction. NDV-GT also expressed porcine αGal antigen, binding to anti-αGal antibodies and triggering a hyperacute rejection reaction, leading to a humoral immune response and complement-dependent cytotoxicity, which damages the tumor vasculature, releasing PAF, thereby inducing platelet aggregation and thrombus formation, ultimately blocking tumor blood vessels and promoting apoptosis. At the molecular level, NDV-GT inhibited the PI3K-Akt pathway, reducing Akt activity and phosphorylation, triggering apoptotic cascades, and suppressing tumor cell proliferation by reducing IKK and NF-κB phosphorylation. Thus, NDV-GT disrupted survival signals, inducing apoptosis and tumor regression.

See also Figure 2 and Table S3.

A

| Patient number	Tumor type	Age (years)	Gender	Stage	Previous lines of therapy	Metastatic tumor sites	Sum LD (cm)	IF for NDV and αGal in tumor tissue*	α1,3GT-PCR in serum (Day 7 after injection)	DC* (im RECIST)	DC Duration (month)
1	Hepatocellular Carcinoma	47	F	IV	2	4	10.2	NA	POS	PR	10
2	Ovarian cancer	47	F	IV	2	6	44.3	POS	POS	PR	12
3	Ovarian cancer	47	F	IV	1	5	31.5	NA	POS	SD	6
4	Rectal cancer	65	M	IV	8	2	3.3	NA	POS	SD	20
5	Lung cancer	51	M	IVa	5	3	4.6	NA	POS	PR	9
6	Lung cancer	51	M	IVa	2	1	2.2	NA	POS	PR	> 32
7	Lung cancer	58	M	IV	3	1	3.8	NA	POS	PR	8
8	Breast cancer	66	F	IV	16	2	7.1	NA	POS	SD	5
9	Breast cancer	62	F	IV	12	4	9	NA	POS	SD	4
10	Esophageal cancer	66	M	IV	2	3	8.0	POS	POS	SD	7
11	Melanoma	29	F	III	2	1	4.2	POS	POS	SD	> 32
12	Hepatocellular Carcinoma	33	M	IV	3	4	14.8	NA	POS	PD	NA
13	Cervical cancer	58	F	IV	3	1	4.6	NA	POS	CR	> 6
14	Cervical cancer	56	F	IIIb	4	2	1.5	NA	POS	SD	12
15	Cervical cancer	54	F	IV	3	5	19.0	NA	POS	PR	> 36
16	Ovarian cancer	51	F	IV	12	2	2.4	NA	POS	SD	>33
17	Ovarian cancer	65	F	IV	2	3	16.1	NA	POS	SD	9
18	Rectal cancer	35	M	IV	7	12	11	NA	POS	PR	3
19	Hepatocellular Carcinoma	43	M	IV	2	8	6.9	NA	POS	PD	3
20	Cervical cancer	37	F	IV	3	2	6	NA	POS	SD	>29
21	Ovarian cancer	50	F	IV	3	2	2.2	NA	POS	SD	>25
22	Ovarian cancer	69	F	IV	5	2	4	NA	POS	PR	14
23	Rectal cancer	67	M	IV	2	2	3	NA	POS	SD	>29

B
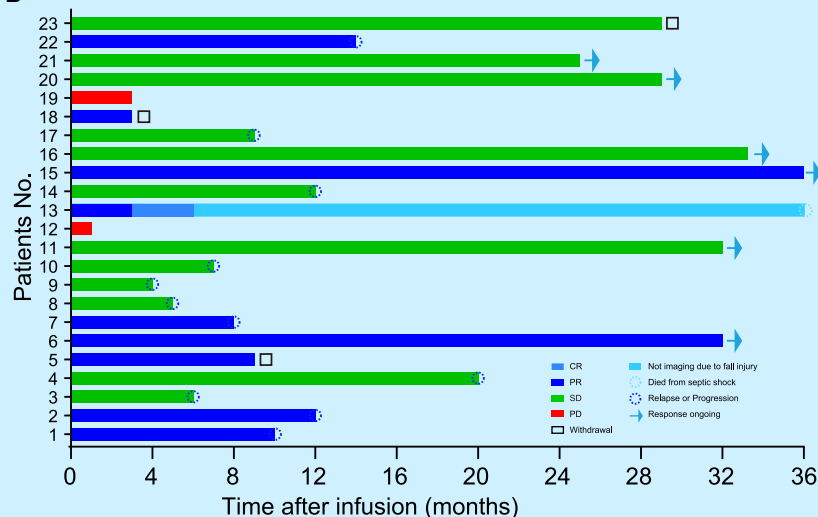
C
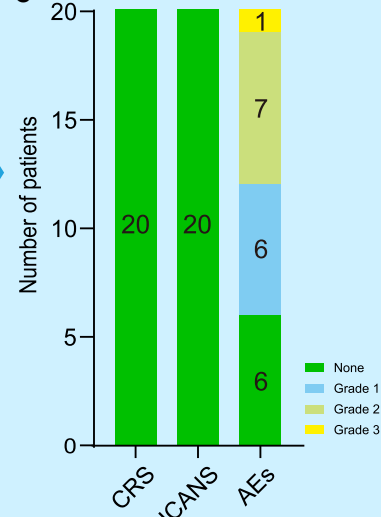
Figure 4. NDV-GT potently inhibited tumor progression in patients with multiple advanced cancers without serious toxicity

(A) Patient characteristics and clinical responses. P5, P18, and P23 withdrew from the clinical study due to the COVID-19 pandemic. LD, longest diameter of tumor; IF, immunofluorescence; DC, disease control; NA, not applicable; POS, positive; CR, complete remission; PR, partial remission; SD, stable disease; PD, progressive disease. *Assessment by imRECIST criteria before and after treatment. For information on race and ethnicity of patients, see Table S4.

(B) Treatment response and duration of response after NDV-GT infusion. CR, complete remission; PR, partial remission; SD, stable disease; PD, progressive disease.

(C) Occurrence of CRS, immune effector cell-associated neurotoxicity syndrome (ICANS), and adverse events (AEs) after treatment.

See also Figures 5, 6, 7, S4, S5, S6, and S7 and Tables S4 and S5.

supported the safety and efficacy of NDV-GT treatment in humans, representing an important step toward its clinical translation.

As shown in Figure 5, P1 presented with multiple primary HCCs and metastatic HCC nodules in the lungs, which decreased in size and even disappeared following 1.5 months

of treatment with NDV-GT (Figures 5A and 5B). Additionally, the NDV-GT treatment significantly reduced the AFP level (Figure 5C), indicating that tumor progression had been suppressed. Furthermore, analysis of immune indices post-treatment revealed that NDV-GT potentiated adaptive immunity, reactivated
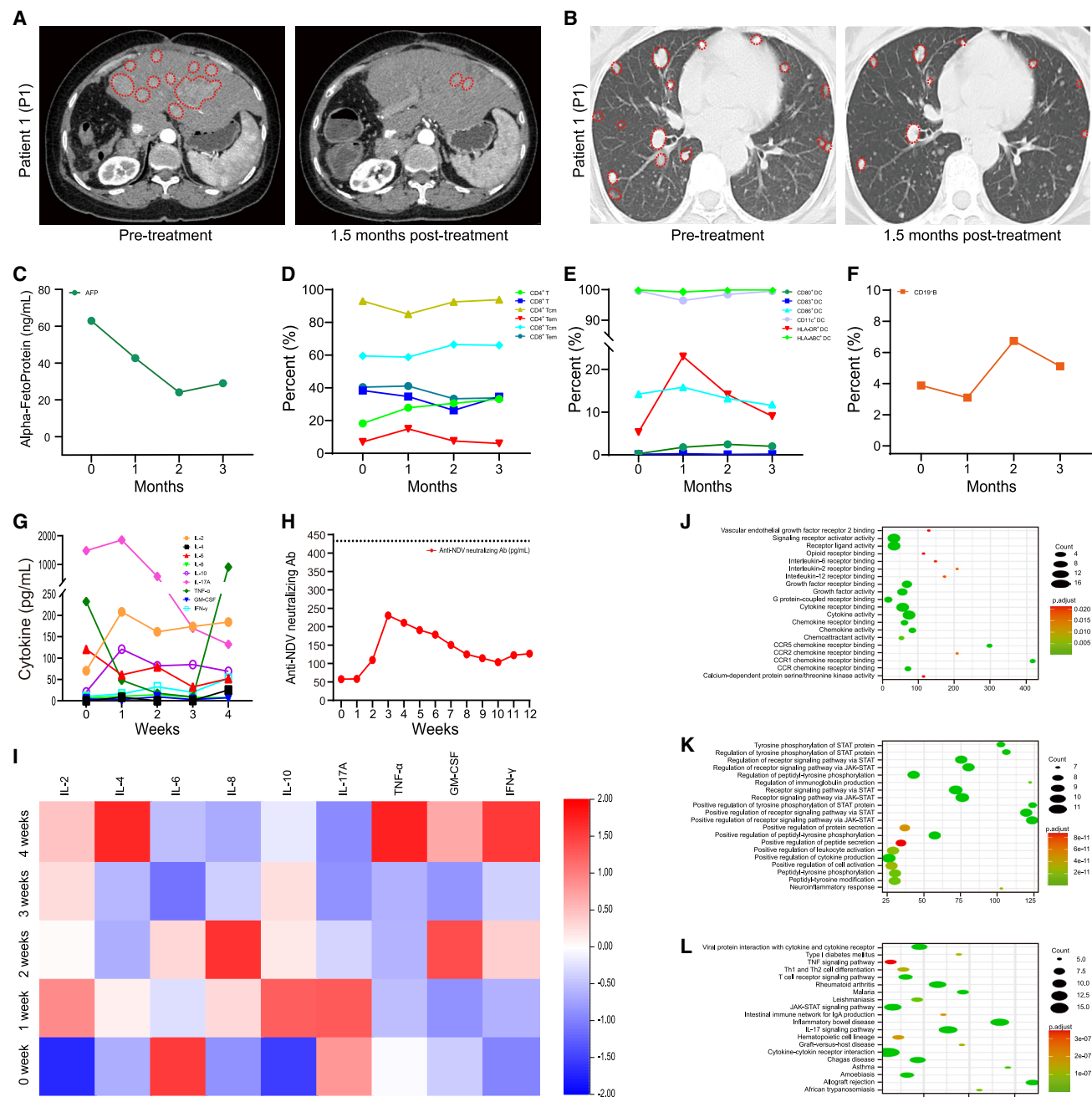
Figure 5. Clinical outcomes of NDV-GT treatment in a refractory HCC patient (P1) with lung metastasis

(A and B) Computed tomography (CT) images of primary HCC in the liver (A) and metastatic HCC in the lungs (B) in P1 before and after 1.5 months of NDV-GT treatment, with tumor lesions indicated by red dashed circles. (A) CT images before treatment displayed multiple diffuse nodules of varying sizes within the liver (indicated by red dashed circles). After 1.5 months of NDV-GT treatment, CT reexamination revealed that most of the nodules disappeared, and only a small part of the reduced mass remained. (B) CT images before treatment demonstrated extensive metastasis of primary liver cancer to both lungs. Following 1.5 months of NDV-GT treatment, a subsequent CT examination showed significant shrinkage of the mass, along with the disappearance of several nodules.

(C) AFP levels during treatment.

(D–F) Flow cytometric profiling of T cell subtypes, including CD4^{+} T cells, CD8^{+} T cells, CD4^{+} Tcm cells, CD8^{+} Tcm cells, CD4^{+} Tem cells, and CD8^{+} Tem cells (D), dendritic cell (DC) maturation (E), and CD19^{+} B lymphocytes (F).

(G) Levels of various cytokines, including IL-2, IL-4, IL-6, IL-8, IL-10, IL-17A, TNF-α, granulocyte-macrophage colony-stimulating factor (GM-CSF), and IFN-γ. These tests were obtained at various time points corresponding to different treatment durations (0, 1, 2, 3, and 4 weeks).

(H) Assessment of anti-NDV neutralizing antibody levels before, during, and after treatment. The dashed lines indicate the upper limit of the normal control value range.

(legend continued on next page)

the immune memory system, alleviated immunosuppression or immune escape, triggered natural anti-tumor immunity, and exerted humoral and cellular immunotherapies (Figures 5D–5F and S5). The treatment also promoted cytokine secretion against tumors and immune escape without inducing cytokine release syndrome (CRS) (Figure 5G). Moreover, NDV-GT did not affect blood indices or kidney function, except for a slight increase in inflammation (Table S5), thus indicating its biosafety.

Importantly, the titer of anti-NDV neutralizing antibody in the blood of the patient post-treatment was slightly higher than that before treatment but still within the normal control value range (Figure 5H). Cytokine array analysis further confirmed cytokine activation and revealed that the activated cytokines were involved in the positive regulation of the JAK-STAT signaling pathway, which regulated the interactions between viral proteins and cytokines/cytokine receptors (Figures 5I–5L; Table S6). Survival analyses based on differences in overall response (OR) showed that NDV-GT effectively treated HCC patients who rapidly achieved PR and remained stable for 10 months (Figure 4B).

In Figure 6, we present P2, who had extensive abdominal metastases originating from ovarian cancer. The results observed in P2 were consistent with those in P1, as demonstrated in Figures 6A–6K and S6 and Tables S5 and S7. Moreover, posttreatment analysis of the ovarian cancer tissue from P2 revealed substantial proliferation of NDV-GT and αGal expression (Figure 6L). This expression elicited a hyperacute rejection response, which in turn promoted thrombosis (Figures 6M and 6N). Additionally, there was significant infiltration of T lymphocytes in the tumor tissue (Figures 6O and 6P), which resulted in an obvious cascade amplification oncolytic reaction, contributing to the successful shrinkage and even disappearance of ovarian tumor (Figure 6A). Furthermore, P2 demonstrated a rapid PR for a duration of 12 months with an overall survival (OS) of 17 months, as assessed by imRECIST (Figure 4B).

In Figure 7, P13 was diagnosed with advanced cervical cancer with iliac crest metastasis, presenting extensive bone destruction, particularly in the sacrum, bilateral iliac bones, and acetabulum, and had previously undergone radiotherapy and chemotherapy. Following 3 months of combined intravenous and peritoneal injections of NDV-GT, a PET-CT scan at the 6-month follow-up revealed a resolution of bone metastases (Figure 7A). Achieving a PR for 3 months, followed by a CR for another 3 months (Figure 4B), P13 experienced substantial relief from bone pain, with analgesic use gradually reduced until no longer needed. Maintaining over 6 months of progression-free survival (PFS) and an OS of 36 months, the patient, unfortunately, succumbed to septic shock, with further imaging follow-up not possible due to a fall.

P14, diagnosed with advanced cervical cancer with pelvic lymph node metastasis involving retroperitoneal lymph nodes in the middle and lower abdomen, had previously undergone radio-

therapy, chemotherapy, and targeted therapy. Following 3 months of combined intravenous and intraperitoneal NDV-GT injections, PET-CT scans revealed a significant reduction in the size of pelvic metastatic lymph node lesions, with most disappearing (Figure 7A). Remaining stable for 12 months (Figure 4B), P14 also reported a decrease in abdominal pain following treatment. After maintaining a 12-month period of SD, P14 experienced relapse and subsequently transitioned to an alternative treatment.

P15, diagnosed with advanced cervical cancer with iliac crest metastasis involving bone destruction in the left sacrum and pelvic lymph node metastasis, initially received radiotherapy and chemotherapy. Following a 3-month regimen of combined intravenous and intraperitoneal NDV-GT administration, PET-CT scans revealed a remarkable reduction or complete resolution of bone metastatic lesions and pelvic metastatic lymph nodes (Figure 7A). P15 experienced significant alleviation of bone pain, allowing for the cessation of analgesic use, and maintained a PR for 36 months (Figure 4B), remaining alive. At the time of manuscript submission, P15 has achieved a PFS of 36 months, with OS not yet reached.

By contrast, the current National Comprehensive Cancer Network Guidelines (NCCN) for second-line treatment of advanced cervical cancer, as seen in the Keynote-158 study, reported median PFS ranging from 2.1 to 5.1 months and median OS from 9.4 to 21.9 months across different drugs.[56,57] Additionally, the adverse effects of NDV-GT treatment were milder, with a lower incidence of adverse events among patients (Table S4). By contrast, patients receiving treatments recommended by current NCCN guidelines often experience adverse effects such as pruritus, fatigue, and diarrhea, with some developing severe grade 3–4 adverse reactions. In the Keynote-158 study,[56,57] the incidence of any-grade adverse events reached 68%, while in the CheckMate 358 study,[58] the incidence of severe treatment-related adverse events (TRAEs) was 16%.

The expression levels of CD4+ T cells, CD8+ T cells, CD4+ central memory T cells (CD4+ Tcm), CD8+ central memory T cells (CD8+ Tcm), and dendritic cells (DCs) in the peripheral blood of P13–P15 increased (Figures 7B–7G). Notably, no CRS was observed in P13–P15 (Figures 4C and 7H–7J). During the treatment period, IL-2 and IFN-γ were secreted at high levels, indicating the activation of anti-tumor immunity (Figures 7H–7J). No significant changes in anti-NDV neutralizing antibodies were detected before and after treatment (Figures 7K–7M; Table S5).

As shown in Figure S4, P6 was a lung cancer patient with brain metastases who relapsed after surgery, chemotherapy, and targeted therapy. This patient received continuous intravenous treatment with NDV-GT for 3 months and achieved PR and has remained stable for 32 months (Figures 4A, 4B, S4A, S4B, and S4E; Table S5). Additionally, P10 was diagnosed with multiple rib and lymph node metastases of esophageal cancer. After surgery and radiotherapy, the disease progressed. The patient was treated with intravenous injection of NDV-GT and experienced

---

(I) Heatmap of cytokines.

(J–L) GO enrichment and KEGG enrichment analyses of cytokines collected at various treatment time points (0 and 1 month) to assess the secretion of cytokines by NDV-GT-infected tumor cells (J) and their role in regulating receptor signaling pathways via JAK-STAT (K), as well as their involvement in viral protein interaction with cytokines and cytokine receptors (L).

See also Figures S5 and S7 and Tables S4, S5, and S6.
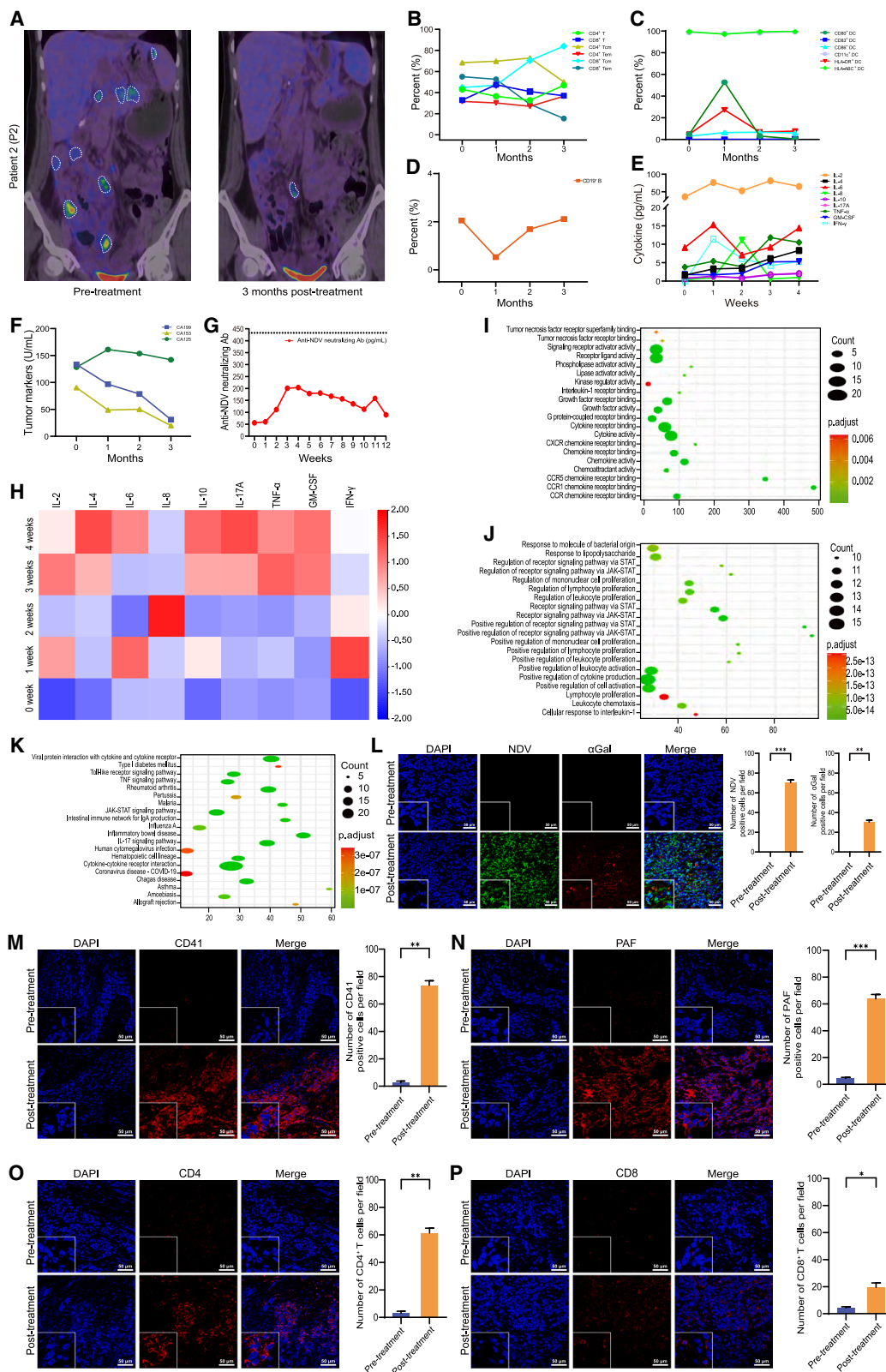
(legend on next page)

SD for 7 months (Figures 4A, 4B, S4A, S4C, and S4F; Table S5). P11 had malignant melanoma with lymph node metastasis. Prior to enrollment, she had undergone surgical treatment and targeted therapy. She received intravenous injection of NDV-GT for 3 months, leading to a 4-month period of stable condition (Figures 4A, 4B, S4A, S4D, and S4G; Table S5). She then underwent surgery to remove the remaining metastases. Currently, the patient has remained stable for over 32 months.

In addition, the titers of anti-NDV neutralizing antibody in the peripheral blood of P6, P10, and P11 only showed a slight increase post-treatment, remaining within the normal control value range (Figures S4H–S4J). Furthermore, no significant correlation was observed between antibody titers and NDV-GT replication, biosafety (Table S5), or oncolytic efficacy. PCR detection on day 7 post-injection after each treatment indicated viral persistence (Figures S7B–S7F). Environmental shedding was undetectable, indicating that NDV-GT was harmless and environmentally friendly (Figures S7G–S7P). Collectively, these data from 20 patients with advanced cancers across various organ sites suggested that successful NDV-GT treatment led to similar responses regardless of the tumor type.

DISCUSSION

As a natural OV, NDV directly infects, lyses, and kills tumor cells via specific interactions with ganglioside-sialic acid receptors, inducing cell apoptosis and leading to tumor ischemia and necrosis by starving tumors.[59,60] Beyond its direct oncolytic effects, NDV can also activate specific or non-specific anti-tumor immune responses, trigger host tumor rejection responses,[61,62] induce specific immune memory effects, and alleviate immunosuppressive microenvironments by promoting antigen presentation, T lymphocyte infiltration, and cytokine secretion.[63,64] Despite these properties, NDV still has inherent limitations, including limited anti-cancer efficacy, low propagation rates, antiviral immune responses, transient immune responses, and potential damage to healthy tissues.

This study aimed to address the limited anti-tumor effect of OVs in eliminating tumor cells and tissues. We genetically engineered a recombinant NDV-GT that retained NDV's tumor-selective replication and oncolytic properties while encoding porcine αGal antigen. The insertion of the α1,3GT gene into NDV enabled infected tumor cells to express exogenous αGal antigen, eliciting a rapid and robust humoral and cellular immune response. This strategy amplified immune responses and triggered ischemic necrosis by disrupting neovascularization, occluding blood vessels, and generating local inflammation and thrombus formation. NDV-GT spread rapidly within tumor tissues, driven by fusion protein and hemagglutinin-neuraminidase protein, with diffusion peaking at 72 h post-injection, influenced by stroma density, vascularization, and immune cell infiltration.[65–67] Reduced collagen fibrils and matrix metalloproteinase production facilitated viral spread,[68] while immune-mediated clearance, initiated by natural killer (NK) cells, CD8+ T cells, IFN responses, and antiviral antibodies, eliminated the virus within approximately 14 days, potentially limiting antitumor efficacy.[62,69,70] Optimizing viral persistence remains crucial for enhancing therapeutic outcomes. Our findings, along with prior studies, demonstrated NDV's selective cytotoxicity in liver cancer, ovarian cancer, cervical cancer, esophageal cancer, and malignant melanoma, with minimal toxicity to normal cells. Preliminary clinical trials confirmed NDV's tumor specificity with no severe adverse events, supporting its potential as a promising OV therapy.

To further explore NDV-GT's oncolytic potential and underlying mechanisms, the CRISPR-Cas9 technology was first used to establish a primary liver cancer model in monkeys.[46] Systematic experiments confirmed that NDV-GT, encoding porcine αGal antigen, significantly enhanced oncolysis, elicited immune responses, reversed immunosuppression, and triggered immune cascades while inhibiting the Akt-IKK-NF-κB pathway to mediate apoptosis, leading to significant liver tumor regression. Subsequently, a pilot clinical study in 20 advanced cancer patients demonstrated the safety of intravenous NDV-GT, with no significant side effects, viral shedding, or transmission to poultry,

Figure 6. Clinical outcomes of NDV-GT treatment in a refractory ovarian cancer patient (P2) with metastasis
(A) Positron emission tomography-computed tomography (PET-CT) images of primary ovarian cancer with abdominal metastasis in P2 before and after 3 months of NDV-GT treatment. Tumor lesions indicated by white dashed circles.
(B–D) FCM analysis of T cell subtypes (B), DC maturation (C), and CD19+ B lymphocytes (D) by FCM.
(E) The levels of various cytokines, including IL-2, IL-4, IL-6, IL-8, IL-10, IL-17A, TNF-α, GM-CSF, and IFN-γ, were assessed at multiple time points corresponding to different treatment durations (0, 1, 2, 3, and 4 weeks).
(F) Levels of tumor markers (CA125, CA153, CA199) during treatment.
(G) Levels of anti-NDV neutralizing antibodies were measured before treatment, during treatment, and after treatment. The dashed lines indicate the upper limit of the normal control value range.
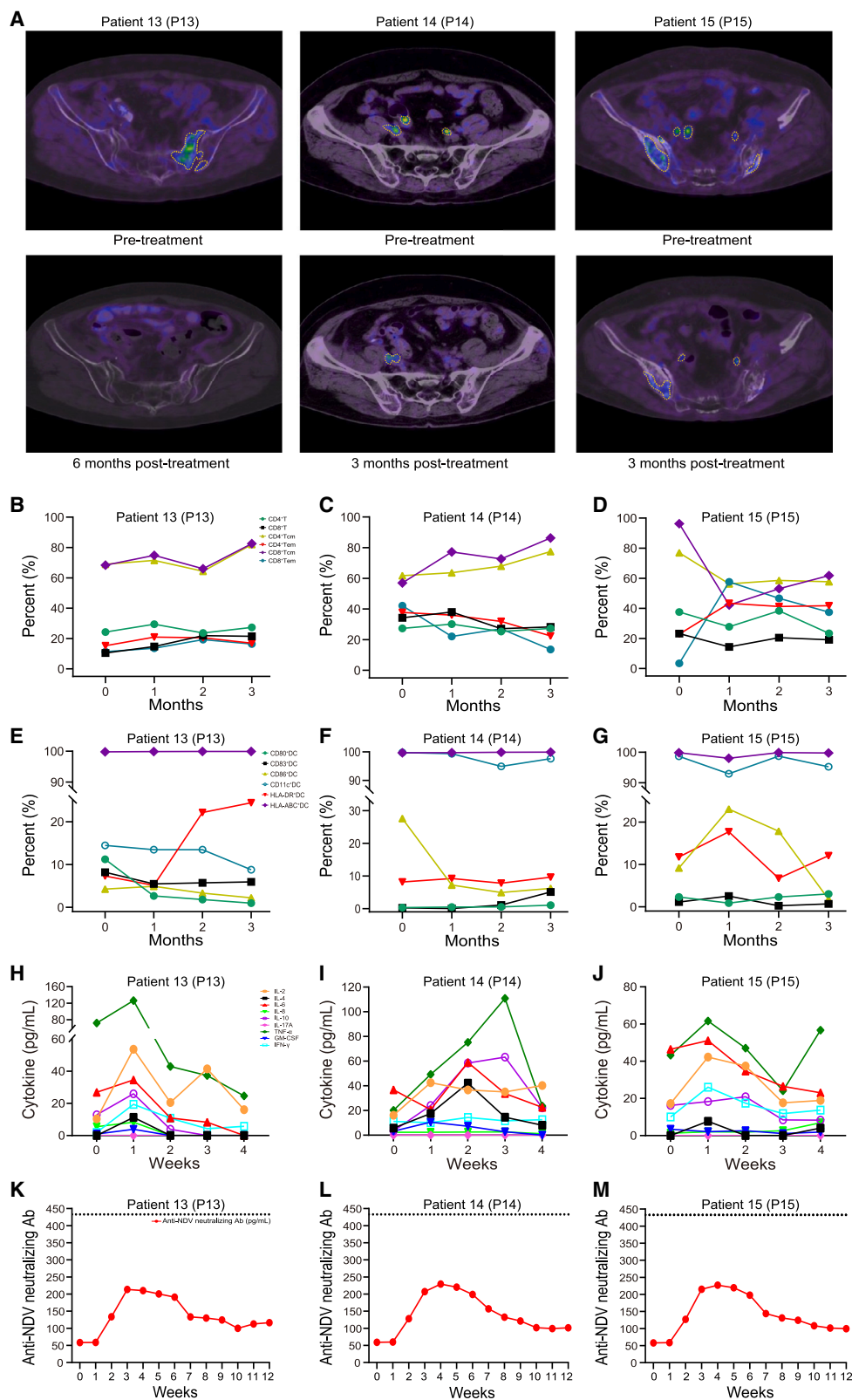(H) Heatmap of cytokines.
(I–K) GO enrichment and KEGG enrichment analyses were conducted on cytokines collected at different treatment time points (0 and 1 month) to assess the secretion of cytokines by NDV-GT-infected tumor cells (I), their role in regulating the receptor signaling pathway via JAK-STAT (J), and their involvement in viral protein interaction with cytokines, cytokine receptors, and the activation of the Toll-like receptor signaling pathway (K).
(L) At the end of 3 months of treatment, the patient underwent minimally invasive laparoscopic surgery for biopsy of the residual peritoneal lesion. LCSM images and quantitative data of NDV and αGal were obtained from both pre- and post-treatment tumor tissues of P2. Notably, in the post-treatment tumor tissues, NDV expression was visualized through green fluorescence, while αGal was indicated by red fluorescence. Scale bars, 50 μm. 400× and 1,000× for the small box. Data are expressed as mean ± SD (n = 3 views), **p < 0.01 and ***p < 0.001.
(M–P) LCSM images and quantitative data for CD41 (M) and PAF (N), both represented by red fluorescence, were used to visualize thrombus formation. Higher expressions of CD41 (M) and PAF (N) in the post-treatment tumor tissues were indicative of a robust hyperacute rejection response. Additionally, increased CD4+ T cells (O) and CD8+ T cells (P) infiltration, represented by red fluorescence, suggested a cascade amplification of the immune response. Scale bars, 50 μm. 400× and 1,000× for the small box. Data are expressed as mean ± SD (n = 3 views), *p < 0.05, **p < 0.01, and ***p < 0.001.
See also Figures S6 and S7 and Tables S4, S5, and S7.

A Patient 13 (P13) Patient 14 (P14) Patient 15 (P15)

Pre-treatment Pre-treatment Pre-treatment

6 months post-treatment 3 months post-treatment 3 months post-treatment

(legend on next page)

thus minimizing cross-species risks. However, despite this safety profile, appropriate biosafety measures should be considered to prevent environmental spread. Subjects working with or owning birds or poultry should avoid contact with these host species for a period post-injection to reduce potential environmental impact on susceptible species.[71,72]

Interestingly, consistent tumor regression mechanisms were observed between monkeys and humans, with stable B cell proportions and minimal changes in neutralizing antibody levels, suggesting that the role of neutralizing antibodies and seroconversion in oncolytic virotherapy remains unclear. In our clinical trial, PCR detection on day 7 post-injection indicated viral persistence, implying incomplete neutralizing antibody formation, likely due to weak immunogenicity or an immunosuppressive state, thereby supporting long-term, repeated NDV-GT administration. Paralleling these findings, a recent glioblastoma study demonstrated similar immune activation with local injection, with both approaches leading to tumor necrosis and cellular immunity.[14] NDV-GT's enhancement of humoral immunity suggests that herpes simplex virus (HSV)- and NDV-based therapies may have complementary roles in different clinical settings, expanding NDV-GT's therapeutic potential and offering valuable insights into the combined use of viral therapies in cancer treatment.

Limitations persist despite our pilot interventional clinical trial in humans confirming the clinical feasibility of NDV-GT usage. While the initial safety profile is promising, more patients and extended post-infusion observation are necessary to fully evaluate its safety and efficacy. The small sample size, typical of an interventional clinical trial, may not adequately reflect broader efficacy, while the short follow-up limited the assessment of long-term outcomes, such as response durability, late-onset adverse events, or tumor recurrence. Additionally, the immunosuppressive tumor microenvironment, including residual regulatory T cells (Tregs) and myeloid-derived suppressor cells (MDSCs) accumulation, might continue limiting OV efficacy, with tumor cells evading infection by downregulating viral targets, interfering with IFN signaling, or overexpressing programmed death-ligand 1 (PD-L1).[73,74] Future research should focus on overcoming these resistance mechanisms to enhance viral therapy.

In this study, we developed a strategy for targeted OV therapy using reverse genetic technology, combining the benefits of hy-

peracute rejection with NDV's natural oncolysis. This two-in-one approach, without using a virus harmful to humans, simplified the manufacturing process, shortened preparation time, reduced production costs, and increased the safety and efficacy of NDV-GT. Meanwhile, unlike conventional therapy, patients may benefit after receiving NDV-GT, resulting in improved OS, even after starting another therapy.[1] These advantages are especially important for gene-engineered OVs, where both virus preparation and reverse genetic processes are typically required. Additionally, locus-specific integration enhanced the homogeneity of NDV-GT, allowing the development of versatile OV products. We successfully demonstrated the feasibility of this technology from bench to bedside, confirming its high safety and efficacy in clinical trials. This innovative OV strategy addresses current barriers, showing great potential for hyperacute rejection-mediated, gene-specific targeting in immunovirotherapy.

As NDV-GT advanced clinically, we further refined the trial design. While the initial 2020 clinical trial protocol included a traditional Chinese medicine component, we excluded this component in the 2022 update to enhance scientific rigor and ensure an independent evaluation of NDV-GT's efficacy. Recognizing the potential efficacy of NDV-GT across multiple cancers, we expanded its application to various solid tumors to validate its broad applicability. Currently, phase II–III clinical trials for diverse malignancies are under application, marking progress in NDV-GT's clinical development by evaluating efficacy and safety and exploring biomarkers and combination therapies to enhance treatment outcomes and advance personalized strategies, ultimately benefiting more patients.

RESOURCE AVAILABILITY

Lead contact
Requests for further information and resources should be directed to and will be fulfilled by the lead contact, Yongxiang Zhao (zhaoyongxiang@gxmu. edu.cn).

Materials availability
This study did not generate new, unique reagents.

Data and code availability
- All data reported in this paper will be shared by the lead contact upon request.
- This paper does not report original code.

Figure 7. Clinical outcomes of NDV-GT treatment in three refractory cervical carcinoma patients (P13, P14, and P15) with metastases

(A) PET-CT images of three representative cervical cancer patients with iliac and/or pelvic lymph node metastases before and after treatment. The yellow dashed circles indicate the tumor lesions. Patient 13 presented PET-CT scans with left iliac metastases from cervical cancer before and after NDV-GT treatment. After 6 months of treatment, bone metastases with lytic bone destruction disappeared. Patient 14 showed a PET-CT scan before and after treatment for cervical cancer with pelvic lymph node metastases. After 3 months of treatment, metastatic lymphatic lesions were significantly shrunken or even disappeared. Patient 15 displayed PET-CT images before and after treatment of cervical cancer with right iliac crest and pelvic lymph node metastases. After 3 months of treatment, the bone metastases of osteolytic bone destruction were significantly reduced, and the metastatic lymphatic lesions were significantly shrunken or even disappeared.

(B–D) FCM profiles for T cell subtypes, including $CD4^+$ T cells, $CD8^+$ T cells, $CD4^+$ Tcm cells, $CD8^+$ Tcm cells, $CD4^+$ Tem cells, and $CD8^+$ Tem cells of three patients.

(E–G) FCM patterns for DC maturation.

(H–J) Levels of various cytokines, including IL-2, IL-4, IL-6, IL-8, IL-10, IL-17A, TNF-α, GM-CSF, and IFN-γ, were assessed at different time points following treatment (0, 1, 2, 3, and 4 weeks).

(K–M) Levels of anti-NDV neutralizing antibody prior to treatment, during treatment, and after treatment. The dashed lines indicate the upper limit of the normal control value range.

See also Figure S7 and Tables S4 and S5.

- Any additional information required to reanalyze the data reported in this paper is available from the lead contact upon request.

AUTHOR CONTRIBUTIONS

L.Z., Y.Z., W.S., and K.Z. conceived and designed this project. L.Z., L.G., B.W., T. Wu, and Z. Deng designed and constructed the NDV-GT. G.X., Xiyu Liu, Z.Z., B.X., F.Y., Y.H., D.Y., Z. Dong, and F.F. performed *in vitro* experiments. L.Z., Y.M., G.J., D.S., Xiuli Liu, Q.L., H.L., C.T., and J.H. established liver cancer cynomolgus monkeys. L.Z., Z.T., S.Z., B.Q., Z.Y., L.Y., J.N., Z.C., Y.L., L.W., Z.M., and M.Z. performed *in vivo* experiments. L.Z., R.F., D.X., J.J., and Z.L. performed sequencing and analyzed the data. B.X., G.X., Y.M., F.Y., F.F., G.J., D.S., Z.T., X.Y., S.S., T. Wang, and W.S. treated patients and collected clinical data. W.S., K.Z., Y.Z., and L.Z. analyzed the data and wrote the manuscript. Y.Z. supervised the project.

DECLARATION OF INTERESTS

The authors declare no competing interests.

STAR★METHODS

Detailed methods are provided in the online version of this paper and include the following:
- KEY RESOURCES TABLE
- EXPERIMENTAL MODEL AND STUDY PARTICIPANT DETAILS
  - Clinical trial design and clinical patient information
  - The exclusion criteria included
  - Clinical response assessment
- METHOD DETAILS
  - Clinical monitoring
  - Assessment and grading of CRS
  - Assessment and grading of neurological toxicity
  - Assessment and grading of AEs
  - Peripheral immune cell subsets determination by flow cytometry
  - Preclinical study
  - Safety evaluation in the preclinical study
- QUANTIFICATION AND STATISTICAL ANALYSIS

SUPPLEMENTAL INFORMATION

Supplemental information can be found online at https://doi.org/10.1016/j.cell.2024.12.010.

REFERENCES

1. Friedman, G.K., Johnston, J.M., Bag, A.K., Bernstock, J.D., Li, R., Aban, I., Kachurak, K., Nan, L., Kang, K.D., Totsch, S., et al. (2021). Oncolytic HSV-1 G207 immunovirotherapy for pediatric high-grade gliomas. N. Engl. J. Med. *384*, 1613–1622. https://doi.org/10.1056/NEJMoa2024947.

2. Desjardins, A., Gromeier, M., Herndon, J.E., Beaubier, N., Bolognesi, D.P., Friedman, A.H., Friedman, H.S., McSherry, F., Muscat, A.M., Nair, S., et al. (2018). Recurrent glioblastoma treated with recombinant poliovirus. N. Engl. J. Med. *379*, 150–161. https://doi.org/10.1056/NEJMoa1716435.

3. Harrington, K., Freeman, D.J., Kelly, B., Harper, J., and Soria, J.C. (2019). Optimizing oncolytic virotherapy in cancer treatment. Nat. Rev. Drug Discov. *18*, 689–706. https://doi.org/10.1038/s41573-019-0029-0.

4. Van Gool, S.W., Makalowski, J., Van de Vliet, P., Van Gool, S., Sprenger, T., Schirrmacher, V., and Stuecker, W. (2023). Individualized multimodal immunotherapy for adults with IDH$_1$ wild-type GBM: A single institute experience. Cancers *15*, 1194. https://doi.org/10.3390/cancers15041194.

5. Todo, T., Ito, H., Ino, Y., Ohtsu, H., Ota, Y., Shibahara, J., and Tanaka, M. (2022). Intratumoral oncolytic herpes virus G47Δ for residual or recurrent glioblastoma: a phase 2 trial. Nat. Med. *28*, 1630–1639. https://doi.org/10.1038/s41591-022-01897-x.

6. Soliman, H., Hogue, D., Han, H., Mooney, B., Costa, R., Lee, M.C., Niell, B., Williams, A., Chau, A., Falcon, S., et al. (2023). Oncolytic T-VEC virotherapy plus neoadjuvant chemotherapy in nonmetastatic triple-negative breast cancer: a phase 2 trial. Nat. Med. *29*, 450–457. https://doi.org/10.1038/s41591-023-02210-0.

7. Ribas, A., Dummer, R., Puzanov, I., VanderWalde, A., Andtbacka, R.H.I., Michielin, O., Olszanski, A.J., Malvehy, J., Cebon, J., Fernandez, E., et al. (2017). Oncolytic virotherapy promotes intratumoral T cell infiltration and improves anti-PD-1 immunotherapy. Cell *170*, 1109–1119.e10. https://doi.org/10.1016/j.cell.2017.08.027.

8. Shalhout, S.Z., Miller, D.M., Emerick, K.S., and Kaufman, H.L. (2023). Therapy with oncolytic viruses: progress and challenges. Nat. Rev. Clin. Oncol. *20*, 160–177. https://doi.org/10.1038/s41571-022-00719-w.

9. Gállego Pérez-Larraya, J., Garcia-Moure, M., Labiano, S., Patiño-García, A., Dobbs, J., Gonzalez-Huarriz, M., Zalacain, M., Marrodan, L., Martinez-Velez, N., Puigdelloses, M., et al. (2022). Oncolytic DNX-2401 virus for pediatric diffuse intrinsic pontine glioma. N. Engl. J. Med. *386*, 2471–2481. https://doi.org/10.1056/NEJMoa2202028.

10. Kaufman, H.L., and Maciorowski, D. (2021). Advancing oncolytic virus therapy by understanding the biology. Nat. Rev. Clin. Oncol. *18*, 197–198. https://doi.org/10.1038/s41571-021-00490-4.

11. Thorne, S.H., Negrin, R.S., and Contag, C.H. (2006). Synergistic antitumor effects of immune cell-viral biotherapy. Science *311*, 1780–1784. https://doi.org/10.1126/science.1121411.

12. Ikeda, K., Ichikawa, T., Wakimoto, H., Silver, J.S., Deisboeck, T.S., Finkelstein, D., Harsh, G.R., Louis, D.N., Bartus, R.T., Hochberg, F.H., et al. (1999). Oncolytic virus therapy of multiple tumors in the brain requires suppression of innate and elicited antiviral responses. Nat. Med. *5*, 881–887. https://doi.org/10.1038/11320.

13. Xu, B., Ma, R., Russell, L., Yoo, J.Y., Han, J., Cui, H., Yi, P., Zhang, J., Nakashima, H., Dai, H., et al. (2018). An oncolytic herpesvirus expressing E-cadherin improves survival in mouse models of glioblastoma. Nat. Biotechnol. *37*, 45–62. https://doi.org/10.1038/nbt.4302.

14. Ling, A.L., Solomon, I.H., Landivar, A.M., Nakashima, H., Woods, J.K., Santos, A., Masud, N., Fell, G., Mo, X., Yilmaz, A.S., et al. (2023). Clinical trial links oncolytic immunoactivation to survival in glioblastoma. Nature *623*, 157–166. https://doi.org/10.1038/s41586-023-06623-2.

15. Bommareddy, P.K., Aspromonte, S., Zloza, A., Rabkin, S.D., and Kaufman, H.L. (2018). MEK inhibition enhances oncolytic virus immunotherapy through increased tumor cell killing and T cell activation. Sci. Transl. Med. *10*, eaau0417. https://doi.org/10.1126/scitranslmed.aau0417.

16. Bommareddy, P.K., Shettigar, M., and Kaufman, H.L. (2018). Integrating oncolytic viruses in combination cancer immunotherapy. Nat. Rev. Immunol. *18*, 498–513. https://doi.org/10.1038/s41577-018-0014-6.

17. Lee, P., and Gujar, S. (2018). Potentiating prostate cancer immunotherapy with oncolytic viruses. Nat. Rev. Urol. *15*, 235–250. https://doi.org/10.1038/nrurol.2018.10.

18. Niemann, J., Woller, N., Brooks, J., Fleischmann-Mundt, B., Martin, N.T., Kloos, A., Knocke, S., Ernst, A.M., Manns, M.P., Kubicka, S., et al. (2019). Molecular retargeting of antibodies converts immune defense against oncolytic viruses into cancer immunotherapy. Nat. Commun. *10*, 3236. https://doi.org/10.1038/s41467-019-11137-5.

19. Xiao, X., Liang, J., Huang, C., Li, K., Xing, F., Zhu, W., Lin, Z., Xu, W., Wu, G., Zhang, J., et al. (2018). DNA-PK inhibition synergizes with oncolytic virus M1 by inhibiting antiviral response and potentiating DNA damage. Nat. Commun. *9*, 4342. https://doi.org/10.1038/s41467-018-06771-4.

20. Selman, M., Ou, P., Rousso, C., Bergeron, A., Krishnan, R., Pikor, L., Chen, A., Keller, B.A., Ilkow, C., Bell, J.C., et al. (2018). Dimethyl fumarate potentiates oncolytic virotherapy through NF-κB inhibition. Sci. Transl. Med. *10*, eaao1613. https://doi.org/10.1126/scitranslmed.aao1613.

21. Breitbach, C.J., Burke, J., Jonker, D., Stephenson, J., Haas, A.R., Chow, L.Q.M., Nieva, J., Hwang, T.H., Moon, A., Patt, R., et al. (2011). Intravenous delivery of a multi-mechanistic cancer-targeted oncolytic poxvirus in humans. Nature *477*, 99–102. https://doi.org/10.1038/nature10358.

22. Ilkow, C.S., Marguerie, M., Batenchuk, C., Mayer, J., Ben Neriah, D.B., Cousineau, S., Falls, T., Jennings, V.A., Boileau, M., Bellamy, D., et al. (2015). Reciprocal cellular cross-talk within the tumor microenvironment promotes oncolytic virus activity. Nat. Med. *21*, 530–536. https://doi.org/10.1038/nm.3848.

23. DePeaux, K., and Delgoffe, G.M. (2024). Integrating innate and adaptive immunity in oncolytic virus therapy. Trends Cancer *10*, 135–146. https://doi.org/10.1016/j.trecan.2023.09.012.

24. Nakao, S., Arai, Y., Tasaki, M., Yamashita, M., Murakami, R., Kawase, T., Amino, N., Nakatake, M., Kurosaki, H., Mori, M., et al. (2020). Intratumoral expression of IL-7 and IL-12 using an oncolytic virus increases systemic sensitivity to immune checkpoint blockade. Sci. Transl. Med. *12*, eaax7992. https://doi.org/10.1126/scitranslmed.aax7992.

25. Park, A.K., Fong, Y., Kim, S.I., Yang, J., Murad, J.P., Lu, J., Jeang, B., Chang, W.C., Chen, N.G., Thomas, S.H., et al. (2020). Effective combination immunotherapy using oncolytic viruses to deliver CAR targets to solid tumors. Sci. Transl. Med. *12*, eaaz1863. https://doi.org/10.1126/scitranslmed.aaz1863.

26. Wang, G., Kang, X., Chen, K.S., Jehng, T., Jones, L., Chen, J., Huang, X.F., and Chen, S.Y. (2020). An engineered oncolytic virus expressing PD-L1 inhibitors activates tumor neoantigen-specific T cell responses. Nat. Commun. *11*, 1395. https://doi.org/10.1038/s41467-020-15229-5.

27. Altomonte, J. (2018). Liver cancer: sensitizing hepatocellular carcinoma to oncolytic virus therapy. Nat. Rev. Gastroenterol. Hepatol. *15*, 8–10. https://doi.org/10.1038/nrgastro.2017.153.

28. Li, R., Zhang, J., Gilbert, S.M., Conejo-Garcia, J., and Mulé, J.J. (2021). Using oncolytic viruses to ignite the tumour immune microenvironment in bladder cancer. Nat. Rev. Urol. *18*, 543–555. https://doi.org/10.1038/s41585-021-00483-z.

29. Senior, M. (2019). Checkpoint inhibitors go viral. Nat. Biotechnol. *37*, 12–17. https://doi.org/10.1038/nbt.4327.

30. Zhang, H., Li, K., Lin, Y., Xing, F., Xiao, X., Cai, J., Zhu, W., Liang, J., Tan, Y., Fu, L., et al. (2017). Targeting VCP enhances anticancer activity of oncolytic virus M1 in hepatocellular carcinoma. Sci. Transl. Med. *9*, eaam7996. https://doi.org/10.1126/scitranslmed.aam7996.

31. Kaufman, H.L., Kohlhapp, F.J., and Zloza, A. (2015). Oncolytic viruses: a new class of immunotherapy drugs. Nat. Rev. Drug Discov. *14*, 642–662. https://doi.org/10.1038/nrd4663.

32. Hemminki, O., Dos Santos, J.M., and Hemminki, A. (2020). Oncolytic viruses for cancer immunotherapy. J. Hematol. Oncol. *13*, 84. https://doi.org/10.1186/s13045-020-00922-1.

33. Stanifer, M.L., Cureton, D.K., and Whelan, S.P.J. (2011). A recombinant vesicular stomatitis virus bearing a lethal mutation in the glycoprotein

gene uncovers a second site suppressor that restores fusion. J. Virol. *85*, 8105–8115. https://doi.org/10.1128/JVI.00735-11.

34. Lin, D., Shen, Y., and Liang, T. (2023). Oncolytic virotherapy: basic principles, recent advances and future directions. Signal Transduct. Target. Ther. *8*, 156. https://doi.org/10.1038/s41392-023-01407-6.

35. Albertini, M.R., Ranheim, E.A., Zuleger, C.L., Sondel, P.M., Hank, J.A., Bridges, A., Newton, M.A., McFarland, T., Collins, J., Clements, E., et al. (2016). Phase I study to evaluate toxicity and feasibility of intratumoral injection of α-gal glycolipids in patients with advanced melanoma. Cancer Immunol. Immunother. *65*, 897–907. https://doi.org/10.1007/s00262-016-1846-1.

36. Zamarin, D., and Palese, P. (2012). Oncolytic Newcastle disease virus for cancer therapy: old challenges and new directions. Future Microbiol. *7*, 347–367. https://doi.org/10.2217/fmb.12.4.

37. Chu, Z., Gao, X., Liu, H., Ma, J., Wang, C., Lu, K., Han, Q., Wang, Y., Wang, C., Adam, F.E.A., et al. (2019). Newcastle disease virus selectively infects dividing cells and promotes viral proliferation. Vet. Res. *50*, 27. https://doi.org/10.1186/s13567-019-0644-0.

38. Dolgin, E. (2021). Pig kidney transplant obscures value of engineered animals. Science *374*, 668–669. https://doi.org/10.1126/science.acx9536.

39. Singh, S., Thompson, J.A., Yilmaz, B., Li, H., Weis, S., Sobral, D., Truglio, M., Aires da Silva, F., Aguiar, S., Carlos, A.R., et al. (2021). Loss of α-gal during primate evolution enhanced antibody-effector function and resistance to bacterial sepsis. Cell Host Microbe *29*, 347–361.e12. https://doi.org/10.1016/j.chom.2020.12.017.

40. Huang, Y., Huang, Y., He, J., Wang, H., Luo, Y., Li, Y., Liu, J., Zhong, L., and Zhao, Y. (2019). Pegylated immunoliposome-loaded endoglin single-chain antibody enhances anti-tumor capacity of porcine alpha 1,3GT gene. Biomaterials *217*, 119231. https://doi.org/10.1016/j.biomaterials.2019.119231.

41. Sianturi, J., Manabe, Y., Li, H.S., Chiu, L.T., Chang, T.C., Tokunaga, K., Kabayama, K., Tanemura, M., Takamatsu, S., Miyoshi, E., et al. (2019). Development of α-Gal-antibody conjugates to increase immune response by recruiting natural antibodies. Angew. Chem. Int. Ed. Engl. *58*, 4526–4530. https://doi.org/10.1002/anie.201812914.

42. Galili, U. (2011). Conversion of tumors into autologous vaccines by intratumoral injection of α-Gal glycolipids that induce anti-Gal/α-Gal epitope interaction. Clin. Dev. Immunol. *2011*, 134020. https://doi.org/10.1155/2011/134020.

43. Hodžić, A., Mateos-Hernández, L., de la Fuente, J., and Cabezas-Cruz, A. (2020). α-Gal-Based vaccines: advances, opportunities, and perspectives. Trends Parasitol. *36*, 992–1001. https://doi.org/10.1016/j.pt.2020.08.001.

44. Saethre, M., Schneider, M.K.J., Lambris, J.D., Magotti, P., Haraldsen, G., Seebach, J.D., and Mollnes, T.E. (2008). Cytokine secretion depends on Gal alpha (1,3) Gal expression in a pig-to-human whole blood model. J. Immunol. *180*, 6346–6353. https://doi.org/10.4049/jimmunol.180.9.6346.

45. Stojdl, D.F., Lichty, B., Knowles, S., Marius, R., Atkins, H., Sonenberg, N., and Bell, J.C. (2000). Exploiting tumor-specific defects in the interferon pathway with a previously unknown oncolytic virus. Nat. Med. *6*, 821–825. https://doi.org/10.1038/77558.

46. Zhong, L., Huang, Y., He, J., Yang, N., Xu, B., Ma, Y., Liu, J., Tang, C., Luo, C., Wu, P., et al. (2021). Generation of *in situ* CRISPR-mediated primary and metastatic cancer from monkey liver. Signal Transduct. Target. Ther. *6*, 411. https://doi.org/10.1038/s41392-021-00799-7.

47. Afshar-Kharghan, V. (2017). The role of the complement system in cancer. J. Clin. Invest. *127*, 780–789. https://doi.org/10.1172/JCI90962.

48. Vollmers, H.P., and Brändlein, S. (2006). Natural IgM antibodies: the orphaned molecules in immune surveillance. Adv. Drug Deliv. Rev. *58*, 755–765. https://doi.org/10.1016/j.addr.2005.08.007.

49. Huai, G., Qi, P., Yang, H., and Wang, Y. (2016). Characteristics of α-Gal epitope, anti-Gal antibody, α1,3 galactosyltransferase and its clinical

exploitation. Int. J. Mol. Med. *37*, 11–20. https://doi.org/10.3892/ijmm.2015.2397.

50. Shaw, S.M., Middleton, J., Wigglesworth, K., Charlemagne, A., Schulz, O., Glossop, M.S., Whalen, G.F., Old, R., Westby, M., Pickford, C., et al. (2019). AGI-134: a fully synthetic α-Gal glycolipid that converts tumors into in situ autologous vaccines, induces anti-tumor immunity and is synergistic with an anti-PD-1 antibody in mouse melanoma models. Cancer Cell Int. *19*, 346. https://doi.org/10.1186/s12935-019-1059-8.

51. Galili, U. (2024). Self-tumor antigens in solid tumors turned into vaccines by α-gal micelle immunotherapy. Pharmaceutics *16*, 1263. https://doi.org/10.3390/pharmaceutics16101263.

52. Wilhite, T., Ezzelarab, C., Hara, H., Long, C., Ayares, D., Cooper, D.K.C., and Ezzelarab, M. (2012). The effect of gal expression on pig cells on the human T-cell xenoresponse. Xenotransplantation *19*, 56–63. https://doi.org/10.1111/j.1399-3089.2011.00691.x.

53. Chandarlapaty, S., Sawai, A., Scaltriti, M., Rodrik-Outmezguine, V., Grbovic-Huezo, O., Serra, V., Majumder, P.K., Baselga, J., and Rosen, N. (2011). AKT inhibition relieves feedback suppression of receptor tyrosine kinase expression and activity. Cancer Cell *19*, 58–71. https://doi.org/10.1016/j.ccr.2010.10.031.

54. Juric, D., Castel, P., Griffith, M., Griffith, O.L., Won, H.H., Ellis, H., Ebbesen, S.H., Ainscough, B.J., Ramu, A., Iyer, G., et al. (2015). Convergent loss of PTEN leads to clinical resistance to a PI(3)Kα inhibitor. Nature *518*, 240–244. https://doi.org/10.1038/nature13948.

55. Hodi, F.S., Ballinger, M., Lyons, B., Soria, J.C., Nishino, M., Tabernero, J., Powles, T., Smith, D., Hoos, A., McKenna, C., et al. (2018). Immune-modified response evaluation criteria in solid tumors (imRECIST): refining guidelines to assess the clinical benefit of cancer immunotherapy. J. Clin. Oncol. *36*, 850–858. https://doi.org/10.1200/JCO.2017.75.1644.

56. Chung, H.C., Ros, W., Delord, J.P., Perets, R., Italiano, A., Shapira-Frommer, R., Manzuk, L., Piha-Paul, S.A., Xu, L., Zeigenfuss, S., et al. (2019). Efficacy and safety of pembrolizumab in previously treated advanced cervical cancer: results from the phase II KEYNOTE-158 study. J. Clin. Oncol. *37*, 1470–1478. https://doi.org/10.1200/JCO.18.01265.

57. Maio, M., Ascierto, P.A., Manzyuk, L., Motola-Kuba, D., Penel, N., Cassier, P.A., Bariani, G.M., De Jesus Acosta, A., Doi, T., Longo, F., et al. (2022). Pembrolizumab in microsatellite instability high or mismatch repair deficient cancers: updated analysis from the phase II KEYNOTE-158 study. Ann. Oncol. *33*, 929–938. https://doi.org/10.1016/j.annonc.2022.05.519.

58. Oaknin, A., Moore, K., Meyer, T., López-Picazo González, J., Devriese, L.A., Amin, A., Lao, C.D., Boni, V., Sharfman, W.H., Park, J.C., et al. (2024). Nivolumab with or without ipilimumab in patients with recurrent or metastatic cervical cancer (CheckMate 358): a phase 1–2, open-label, multicohort trial. Lancet Oncol. *25*, 588–602. https://doi.org/10.1016/S1470-2045(24)00088-3.

59. Li, S., Jiang, Q., Liu, S., Zhang, Y., Tian, Y., Song, C., Wang, J., Zou, Y., Anderson, G.J., Han, J.Y., et al. (2018). A DNA nanorobot functions as a cancer therapeutic in response to a molecular trigger in vivo. Nat. Biotechnol. *36*, 258–264. https://doi.org/10.1038/nbt.4071.

60. Zhang, K., Fang, Y., He, Y., Yin, H., Guan, X., Pu, Y., Zhou, B., Yue, W., Ren, W., Du, D., et al. (2019). Extravascular gelation shrinkage-derived internal stress enables tumor starvation therapy with suppressed metastasis and recurrence. Nat. Commun. *10*, 5380. https://doi.org/10.1038/s41467-019-13115-3.

61. Svensson-Arvelund, J., Cuadrado-Castano, S., Pantsulaia, G., Kim, K., Aleynick, M., Hammerich, L., Upadhyay, R., Yellin, M., Marsh, H., Oreper, D., et al. (2022). Expanding cross-presenting dendritic cells enhances oncolytic virotherapy and is critical for long-term anti-tumor immunity. Nat. Commun. *13*, 7149. https://doi.org/10.1038/s41467-022-34791-8.

62. Schirrmacher, V., van Gool, S., and Stuecker, W. (2019). Breaking therapy resistance: an update on oncolytic Newcastle disease Virus for improvements of cancer therapy. Biomedicines *7*, 7030066. https://doi.org/10.3390/biomedicines7030066.

63. Galili, U., Chen, Z.C., and DeGeest, K. (2003). Expression of alpha-gal epitopes on ovarian carcinoma membranes to be used as a novel autologous tumor vaccine. Gynecol. Oncol. *90*, 100–108. https://doi.org/10.1016/s0090-8258(03)00148-3.

64. Thompson, E.M., Landi, D., Brown, M.C., Friedman, H.S., McLendon, R., Herndon, J.E., Buckley, E., Bolognesi, D.P., Lipp, E., Schroeder, K., et al. (2023). Recombinant polio-rhinovirus immunotherapy for recurrent paediatric high-grade glioma: a phase 1b trial. Lancet Child Adolesc. Health *7*, 471–478. https://doi.org/10.1016/S2352-4642(23)00031-7.

65. Schirrmacher, V., van Gool, S., and Stuecker, W. (2022). Counteracting immunosuppression in the tumor microenvironment by oncolytic Newcastle disease virus and cellular immunotherapy. Int. J. Mol. Sci. *23*, 13050. https://doi.org/10.3390/ijms232113050.

66. Harper, J., Burke, S., Travers, J., Rath, N., Leinster, A., Navarro, C., Franks, R., Leyland, R., Mulgrew, K., McGlinchey, K., et al. (2021). Recombinant Newcastle disease virus immunotherapy drives oncolytic effects and durable systemic antitumor immunity. Mol. Cancer Ther. *20*, 1723–1734. https://doi.org/10.1158/1535-7163.MCT-20-0902.

67. Bazan-Peregrino, M., Garcia-Carbonero, R., Laquente, B., Álvarez, R., Mato-Berciano, A., Gimenez-Alejandre, M., Morgado, S., Rodríguez-García, A., Maliandi, M.V., Riesco, M.C., et al. (2021). VCN-01 disrupts pancreatic cancer stroma and exerts antitumor effects. J. Immunother. Cancer *9*, e003254. https://doi.org/10.1136/jitc-2021-003254.

68. Schirrmacher, V. (2017). Immunobiology of Newcastle disease virus and its use for prophylactic vaccination in poultry and as adjuvant for therapeutic vaccination in cancer patients. Int. J. Mol. Sci. *18*, 1103. https://doi.org/10.3390/ijms18051103.

69. Liu, T.C., Galanis, E., and Kirn, D. (2007). Clinical trial results with oncolytic virotherapy: a century of promise, a decade of progress. Nat. Clin. Pract. Oncol. *4*, 101–117. https://doi.org/10.1038/ncponc0736.

70. Lorence, R.M., Roberts, M.S., O'Neil, J.D., Groene, W.S., Miller, J.A., Mueller, S.N., and Bamat, M.K. (2007). Phase 1 clinical experience using intravenous administration of PV701, an oncolytic Newcastle disease virus. Curr. Cancer Drug Targets *7*, 157–167. https://doi.org/10.2174/156800907780058853.

71. de Swart, R.L., and Belov, G.A. (2023). Advantages and challenges of Newcastle disease virus as a vector for respiratory mucosal vaccines. Curr. Opin. Virol. *62*, 101348. https://doi.org/10.1016/j.coviro.2023.101348.

72. Onnockx, S., Baldo, A., and Pauwels, K. (2023). Oncolytic viruses: an inventory of shedding data from clinical trials and elements for the environmental risk assessment. Vaccines *11*, 1448. https://doi.org/10.3390/vaccines11091448.

73. Goddard, E.T., Linde, M.H., Srivastava, S., Klug, G., Shabaneh, T.B., Iannone, S., Grzelak, C.A., Marsh, S., Riggio, A.I., Shor, R.E., et al. (2024). Immune evasion of dormant disseminated tumor cells is due to their scarcity and can be overcome by T cell immunotherapies. Cancer Cell *42*, 119–134.e12. https://doi.org/10.1016/j.ccell.2023.12.011.

74. Jhunjhunwala, S., Hammer, C., and Delamarre, L. (2021). Antigen presentation in cancer: insights into tumour immunogenicity and immune evasion. Nat. Rev. Cancer *21*, 298–312. https://doi.org/10.1038/s41568-021-00339-z.

Cell
Resource

STAR★METHODS

KEY RESOURCES TABLE

REAGENT or RESOURCE	SOURCE	IDENTIFIER
Antibodies		
PE Human IgG2 Isotype Ctrl Recombinant	Biolegend	Cat# 403605, RRID:AB_3097052
FITC anti-human CD4	Biolegend	Cat# 300538, RRID:AB_2562052
APC anti-human CD8	Biolegend	Cat# 344722, RRID:AB_2075388
APC/Cyanine7 anti-human CD3	Biolegend	Cat# 300318, RRID:AB_314054
CD45RO Monoclonal Antibody (UCHL1), PE-eFluor™ 610, eBioscience	Thermo Fisher Scientific	Cat# 61-0457-41, RRID:AB_2815299
APC anti-human CD197 (CCR7)	Biolegend	Cat# 353214, RRID:AB_10917387
Pacific Blue(TM) anti-human CD19	Biolegend	Cat# 302232, RRID:AB_2073118
FITC anti-human CD80	Biolegend	Cat# 305206, RRID:AB_314502
PE anti-human HLA-DR	Biolegend	Cat# 327008, RRID:AB_893571
APC anti-human CD83	Biolegend	Cat# 305312, RRID:AB_314520
FITC anti-human HLA-A,B,C	Biolegend	Cat# 311404, RRID:AB_314873
PE anti-human CD86	Biolegend	Cat# 305406, RRID:AB_314526
Anti-CD4 antibody [EPR6855]	abcam	Cat# ab133616, RRID:AB_2750883
Anti-CD8 alpha antibody [C8/468]	abcam	Cat# ab233995
Anti-CD31 antibody [EPR3094]	abcam	Cat# ab76533, RRID:AB_1523298
Anti-CD41 antibody [EPR4330]	abcam	Cat# ab134131, RRID:AB_2732852
Mouse Anti-CD105 Monoclonal Antibody, Fluorescein Conjugated, Clone SN6	abcam	Cat# ab11415, RRID:AB_298020
Anti-Newcastle Disease virus antibody	abcam	Cat# ab34402, RRID:AB_776737
alpha-Gal Epitope (Galalpha1-3Galbeta1-4GlcNAc-R), mAb (M86)	Enzo Life Sciences	Cat# ALX-801-090, RRID:AB_2111596
Anti-Perforin antibody [5B10], prediluted	abcam	Cat# ab75573, RRID:AB_1310569
Anti-Granzyme B antibody	abcam	Cat# ab53097, RRID:AB_2114427
Anti-PAF	ZIKER	Cat# ZIKER-1119R
Anti-Fibrinogen alpha chain antibody [EPR2919]	abcam	Cat# ab92572, RRID:AB_10561758
Donkey Anti-Rabbit IgG H&L (Alexa Fluor® 647)	abcam	Cat# ab150075, RRID:AB_2752244
Goat Anti-Chicken IgY H&L (Alexa Fluor® 488) preadsorbed	abcam	Cat# ab150173, RRID:AB_2827653
Goat Anti-Mouse IgG H&L (Alexa Fluor 647) Antibody	abcam	Cat# ab150115, RRID:AB_2687948
Mouse Anti-Actin, beta Monoclonal Antibody, Unconjugated, Clone mAbcam 8226	abcam	Cat# ab8226, RRID:AB_306371
Recombinant Anti-PI3Kinase p85 alpha (phospho Y467) + PI3 Kinase p55 (phospho Y199) Antibody [PI3KY458-1A11]	abcam	Cat# ab278545
Recombinant Anti-PI 3 Kinase p85 alpha antibody [EPR18702]	abcam	Cat# ab191606, RRID:AB_2891324
Phospho-Akt (Ser473) (D9E) XP® Rabbit mAb	Cell Signaling Technology	Cat# 4060, RRID:AB_2315049
Akt Antibody	Cell Signaling Technology	Cat# 9272, RRID:AB_329827
Anti-IKK alpha + IKK beta (phospho S176 + S177) Antibody	abcam	Cat# ab194528
IKK alpha antibody [Y463]	abcam	Cat# ab32041, RRID:AB_733070

(Continued on next page)

Continued

REAGENT or RESOURCE	SOURCE	IDENTIFIER
NFkB p65 (phospho S529) antibody	abcam	Cat# ab97726, RRID:AB_10681170
NFkB p65 antibody [E379]	abcam	Cat# ab32536, RRID:AB_776751
Anti-Caspase-9 (phospho T125) Antibody	abcam	Cat# ab192815
Caspase 9 antibody [E23]	abcam	Cat# ab32539, RRID:AB_725960
Cleaved Caspase-3 (Asp175) Antibody	Cell Signaling Technology	Cat# 9661, RRID:AB_2341188
APC anti-human CD11c	Biolegend	Cat# 980604, RRID:AB_2876773
Goat Anti-Mouse IgG H&L (Alexa Fluor 790)	abcam	Cat# ab175783
Goat Anti-Rabbit IgG H&L (Alexa Fluor 790)	abcam	Cat# ab175781
APC/Fire(TM) 750 anti-human CD20	Biolegend	Cat# 302358, RRID:AB_2572126
Rabbit polyclonal Secondary Antibody to Human IgM - mu chain (HRP)	abcam	Cat# ab97210, RRID:AB_10679521
Rabbit Anti-Human IgG H&L (HRP)	abcam	Cat# ab6759, RRID:AB_955434
Rabbit Anti-Human IgA H&L (HRP)	abcam	Cat# ab8510, RRID:AB_955375
Recombinant Anti-C4b antibody [EPR11203-27]	abcam	Cat# ab181241, RRID:AB_2814770
Complement C3b Monoclonal Antibody (755)	Thermo Fisher Scientific	Cat# MA1-40155, RRID:AB_1073821
Biological samples		
Patient's peripheral blood	The First Affiliated Hospital, Guangxi University of Chinese Medicine	N/A
Patient's urine	The First Affiliated Hospital, Guangxi University of Chinese Medicine	N/A
Patient's stools	The First Affiliated Hospital, Guangxi University of Chinese Medicine	N/A
Chemicals, peptides, and recombinant proteins		
1 × PBS Buffer	Solarbio	Cat# P1020
10 × PBST	Solarbio	Cat# P1033
1 × TBST Buffer	Solarbio	Cat# T1085
Trypsin Digestion solutions, 0.25%. (with phenol red)	Solarbio	Cat# T1360
Native Mouse Fibronectin protein	abcam	Cat# ab92784
Critical commercial assays		
AKT-IN-6	MedChemExp	Cat# HY-19982
BD Pharm Lyse™ Lysing Buffer	BD Biosciences	Cat# 555899
Fetal bovine serum	Gibco	Cat# 10099141
DMEM	Gibco	Cat# 11995065
RPMI 1640	Gibco	Cat# 11875093
SpermRinse	Vitrolife	Cat# 10101
G-1™ PLUS	Vitrolife	Cat# 10128
Stem cell culture medium	Ubigene	Cat# YM-HA-001
Tiletamine Hydrochloride and Zolazepam Hydrochloride for Injection	Virbac	Zoletil®50
Paraformaldehyde (4%)	Biosharp	Cat# BL539A
Opti-MEM	Invitrogen	Cat# 11058021
Pme I Restriction enzymes	New England Biolabs (NEB) Co., LTD.	Cat# R0560L
Cell Counting Kit-8 (CCK-8)	Engreen	Cat# EC008
Platinum™ Taq DNA Polymerase, High Fidelity	Invitrogen	Cat# 11304029
EL-OPD Chromogenic Reagent kit	BBI	Cat# C510018-0500
Test Kit for Antibodies to Newcastle Disease Virus (ELISA)	Jiangsu JingMei Biological CO., LTD	Cat# JM-09205C1

(*Continued on next page*)

Continued

REAGENT or RESOURCE	SOURCE	IDENTIFIER
Test Kit for Monkey IgG Antibodies to Newcastle Disease Virus ELISA	Jianglai Biological CO., LTD	Cat# JL24872
Hematoxylin and Eosin Staining Kit	Yeasen	Cat# 60524ES60
SDS-PAGE gel quick preparation kit	Beyotime	Cat# P0012AC
X-tremeGENE™ HP DNA Transfection Reagent	Roche Co., LTD.	Cat# 6366244001
PureLink™ RNA Micro Scale Kit	Invitrogen	Cat# 12183016
Gel Extraction Kit	OMEGA Co., LTD	Cat# D2500
Plasmid Mini Kit	OMEGA Co., LTD	Cat# D6943
Click-iT™ TUNEL Alexa Fluor™ Imaging Assay	Invitrogen	Cat# C10247
eBioscience™ Annexin V Apoptosis Detection Kit FITC	Invitrogen	Cat# 88-8005-74
Experimental models: Cell lines		
BSR-T7/5	This laboratory	N/A
HepG2	This laboratory	N/A
HO8910	This laboratory	N/A
HeLa	This laboratory	N/A
A549	This laboratory	N/A
TE-10	This laboratory	N/A
SK-MEL-28	This laboratory	N/A
MDA-MB-231	This laboratory	N/A
LS513	This laboratory	N/A
THLE-2	This laboratory	N/A
HUVEC	This laboratory	N/A
IMR-90	This laboratory	N/A
H9C2	This laboratory	N/A
HEK-293T	This laboratory	N/A
H9	This laboratory	N/A
Sperm	Qinzhou Maternal and Child Health Hospital, Ethics Number: QZSFYSL[2024]01, 2024KY0192	N/A
Ovum		N/A
Blastula		N/A
Experimental models: Organisms/strains		
Cynomolgus monkey	Changchun Biotechnology Co., Ltd.	N/A
Oligonucleotides	SOURCE	SEQUENCE
GT- PF	Sangon Biotech (Shanghai) Co., Ltd.	AGGTCCAACTCTGTTTAAACTT AGAAAAAATACGGGTAGAAGT GCCACCATGAATGTCAAA GGA
GT- PR	Sangon Biotech (Shanghai) Co., Ltd.	GAGGATTGCCGCTTGGGTTTA AACTCAGATGTTATTTCTAACC AAATTATACTCTT
LA3000-PF	Sangon Biotech (Shanghai) Co., Ltd.	GTTAGATGCAGCCGGGTCG
LA3300-PR	Sangon Biotech (Shanghai) Co., Ltd.	AATGGGCAGAATCAAAGTA
Software and algorithms		
R (version 3.5.1)	CRAN	https://www.r-project.org/
ImageJ (version 1.7.0)	National Institutes of Health	https://imagej.nih.gov/ij/
GraphPad Prism (version 8.0)	GraphPad Software, La Jolla California, USA	https://www.graphpad.com/
Primer Premier (version 5.0)	Premier Biosoft	http://www.premierbiosoft.com/
Odyssey (version 3.0)	LI-COR	https://www.licor.com/bio/odyssey-dlx/
Kaluza (version 2.1)	Beckman Coulter	https://www.beckman.com/

EXPERIMENTAL MODEL AND STUDY PARTICIPANT DETAILS

Clinical trial design and clinical patient information

This study was an open-label, single-arm clinical trial designed to evaluate the safety and efficacy of NDV-GT in treating relapsed/refractory aggressive malignancies. The clinical protocol has been registered at the Chinese Clinical Trial Registry of WHO (https://www.chictr.org.cn/) (ChiCTR2000031980). The inclusion criteria were as follows: (1) age between 18 and 80 years old, male or female; (2) diagnosis with advanced malignant solid tumors (stages **III-IV**) confirmed by histology/cytology and who lack standard treatment or do not have standard treatment conditions; (3) Child-Pugh liver function rating: A, B; (4) according to the imRECIST of the solid tumor efficacy evaluation criteria, the patient has one of the following conditions: (a) There is a lesion that can be measured by imaging (CT or MRI (magnetic resonance imaging) or PET-CT or B ultrasound), and the longest diameter is $\geq$ 10 mm (if it is a lymph node, the short axis is required to be $\geq$ 15 mm) (brain metastases are not considered as the only measurable lesions); (b) circulating tumor cells that metastasized into the bloodstream tested positive; (5) model of end-stage liver disease (MELD) score < 9 points; (6) no other accompanying anti-tumor therapy; (7) Eastern Cooperative Oncology Group (ECOG) score of $\leq$ 2 and satisfactory major organ functions; (8) the standard of blood routine examination should meet hemoglobin (Hb) $\geq$ 80 g/L, ANC $\geq$ 1.5 $\times$ 10^9 /L, PLT $\geq$ 70 $\times$ 10^9 /L; (9) patients must recover to $\leq$ grade 1 from previous therapeutic toxicity, except for alopecia and grade 2 prior platinum-containing treatment-related neuropathy (CTCAE 5.0). (Methods S1: Clinical trial protocol, related to Figures 4, 5, 6, 7, S4, S5, S6, and S7 and Tables S4, S5, S6, and S7.) Patient demographic information and additional details are summarized in Figure 4A and provided in Table S4.

The exclusion criteria included

(1) patients with a history of allergy to oncolytic viruses and their metabolites or their pharmaceutical excipients (whether active or not); (2) the adverse reactions of previous anti-tumor therapy have not been recovered to CTCAE 5.0 grade evaluation $\leq$ grade 1 (except for toxicities such as hair loss that the researchers judged to have no safety risk); (3) received immunotherapy and had irAE (immune-related adverse events) grade $\geq$ 3; (4) active infections; (5) history of severe cardiovascular disease; (6) patients with mental disorders or poor compliance; (7) pregnant or lactating women.

To preliminarily determine the safety and efficacy of this oncolytic virus therapy, 23 patients who had not previously received oncolytic virus therapy were enrolled in the study. They received an intravenous infusion of 1-3 $\times$ 10^7 PFU/kg of NDV-GT dissolved in 100 mL of 0.9% normal saline once weekly for 8–12 weeks. An NDV-GT dose-escalation trial was designed with 23 patients at dose level 1 (1 $\times$ 10^7 PFU/kg) in the dose-escalation phase. Of these patients, 20 underwent a full dose-escalation test. As the trial progressed, the dose was gradually increased to dose level 2 (1 $\times$ 10^8 PFU/kg) and ultimately to dose level 3 (1 $\times$ 10^9 PFU/kg) in the dose-expansion phase. If unacceptable side effects were observed with the initial dose, a lower dose would be evaluated.

Dose Level	Patients	Dose (PFU/kg)	Volume	# Loci
-1	3	1 $\times$ 10^6	1.0 mL	1-4
1	3 (+3)	1 $\times$ 10^7	1.0 mL	1-4
2	3 (+3)	1 $\times$ 10^8	1.0 mL	1-4
3	3 (+3)	1 $\times$ 10^9	1.0 mL	1-4

Intraperitoneal infusion: 1 $\times$ 10^8 PFU/kg NDV-GT dissolved in 250-500 mL of 0.9% normal saline and administered via intraperitoneal injection once weekly for 8-12 weeks. Prior to enrollment, all patients provided written informed consent in accordance with the Declaration of Helsinki. Standard monitoring followed the NDV-GT injection. The clinical trial was reviewed and approved by the Clinical Research Ethics Committee of the First Affiliated Hospital, Guangxi University of Chinese Medicine (Opinion No.: Lun Audit 2020-009-02). The characteristics, clinical responses, and prior therapies of the patients are detailed in the following section (Figures 4A and 5B).

Considering the ethical requirements and maximizing the interests of the subjects, P1-4 and P12-23 were given intravenous injection of NDV-GT combined with intraperitoneal injection, while P5-11 were given intravenous injection only, according to the patient's condition and informed consent, in order to achieve the optimal effect.

Clinical response assessment

Treatment response was evaluated using the imRECIST criteria. PET-CT, CT, MRI, B-ultrasound, and tumor tissue biopsy were the primary methods applied to assess lesions. The response assessment criteria were as follows: (1) CR: absence of lesions; (2) PR: a reduction in the sum of the longest diameters of baseline lesions by more than 30%; (3) PD: an increase in the sum of the longest diameters of lesions by more than 20% or the appearance of new lesions; (4) SD: a condition that did not meet the criteria for CR, PR, or PD. Response duration was calculated from the initial documentation of response until disease progression, initiation of off-study treatment, or the last documentation of ongoing response.

METHOD DETAILS

Clinical monitoring

After each treatment, each patient's vital signs including body temperature, blood pressure, respiration, and heart rate were closely monitored. No flu-like symptoms such as fever, chills, diarrhea, rhinorrhea, or other discomforts were observed except for mild drowsiness. Routine blood tests and liver and kidney function assays were conducted to assess the safety and toxicity of the oncolytic virus NDV-GT. EDTA anticoagulant-treated peripheral venous blood samples were collected for routine blood tests before medication and at 0, 1, 2, and 3 months after treatment initiation. Additionally, 3 mL of non-anticoagulant peripheral blood was collected in dry vacuum tubes, and AFP, CA199, CA125, CA153, liver function, and kidney function were examined by the clinical laboratory of the First Affiliated Hospital of Guangxi Medical University.

Assessment and grading of CRS

Peripheral venous blood samples were collected from patients before treatment and 1, 2, 3, and 4 weeks after treatment initiation. Non-anticoagulant peripheral venous blood was collected in vacuum drying tubes at 2000 rpm. Serum was harvested after 15 min of centrifugation and sent to RayBiotech for the determination of cytokines including IL-2, IL-4, IL-6, IL-8, IL-10, IL-17A, TNF-α, GM-CSF, and IFN-γ. GO analysis and KEGG signal pathway enrichment analyses were performed. CRS was assessed and graded according to the National Cancer Institute Common Terminology Criteria for Adverse Events (NCI-CTCAE) version 5.0 in combination with other methods.

Assessment and grading of neurological toxicity

Neurotoxicities were evaluated and graded according to the NCI-CTCAE version 5.0. In the event of CRS symptoms such as fever, hypotension, and capillary leak syndrome or any other AEs, patients would be closely monitored for signs of neurotoxicity, including dysphasia, seizures, tremors, or encephalopathy.

Assessment and grading of AEs

All patients were hospitalized and closely monitored after receiving NDV-GT treatment. Physical and clinical laboratory examinations were conducted during hospitalization to assess any toxic side effects of the treatment. Any AEs that occurred after NDV-GT infusion were also recorded during this period. Severe AEs were required to be reported to the Medical Ethics Committee of the First Affiliated Hospital, Guangxi University of Chinese Medicine within 24 hours of occurrence. The patients were followed up after the infusion and monitored monthly thereafter for disease progression and any toxicities. The grading of AEs was done using the NCI-CTCAE version 5.0. A summary of all the AEs is provided in Table S4.

Peripheral immune cell subsets determination by flow cytometry

The effect of the oncolytic virus NDV-GT on immune cells *in vivo* was evaluated by collecting 4 mL of peripheral venous blood in EDTA anticoagulant-containing tubes from patients before medication and 4, 8, and 12 weeks after treatment. The percentages of various immune cells were detected by flow cytometry including CD4$^+$ T cells, CD4$^+$ Tcm, CD4$^+$ Tem, CD8$^+$ T cells, CD8$^+$ Tcm, CD8$^+$ Tem, DC, and B cells. Reagents and materials are given in the key resources table.

Two mL of fresh peripheral blood was collected from each patient and added into the EDTA anticoagulation tube. Subsequently, 1 × red blood cell lysis buffer was added and placed at room temperature for 15 min with vortexing once every 5 min, followed by centrifugation at 2500 rpm for 5 min. After discarding the supernatant, the cells in each tube were re-suspended in 10 mL of PBS containing 1% FBS and then centrifuged at 2500 rpm for 5 min. The supernatant was removed, and the cell concentration was adjusted to 1 × 10^7/mL with 100 μL cell suspension/tube.

CD4$^+$ T cells: CD3$^+$ CD4$^+$
CD8$^+$ T cells: CD3$^+$ CD8$^+$
CD4$^+$ effective memory T cells: CD3$^+$ CD4$^+$ CD45RO$^+$ CCR7$^-$
CD4$^+$ central memory T cells: CD3$^+$ CD4$^+$ CD45RO$^+$ CCR7$^+$
CD8$^+$ effective memory T cells: CD3$^+$ CD8$^+$ CD45RO$^+$ CCR7$^-$
CD8$^+$ central memory T cells: CD3$^+$ CD8$^+$ CD45RO$^+$ CCR7$^+$
DC: CD80$^+$, CD83$^+$, CD86$^+$, HLA-DR$^+$, HLA-ABC$^+$, CD11c$^+$
B cells: CD19$^+$ CD20$^+$

Cells were first incubated at 4°C for 30 min in the dark. Subsequently, they were resuspended in PBS containing 1% FBS and centrifuged at 2500 rpm for 5 min. The supernatant was discarded, and the cells were gently blotted dry with absorbent paper. The cells were then resuspended in 300 μL of PBS containing 1% fetal bovine serum (FBS) and passed through a 200-mesh filter to remove any clumps or aggregates. The filtered cells were ready for flow cytometry (Beckman).

Preclinical study

Viral strain, plasmid construction and virus rescue

NDV parental strain plasmid (LaSota), and three helper plasmids (pCI-NP, pCI-P and pCI-L) were preserved in our laboratory. The Primer Premier 5.0 design software was employed to design the overlap PCR primer using the NDV GenBank sequence, and the overlap PCR method with the single restriction enzyme site in the $\alpha1,3GT$ gene sequence was used to expand the $\alpha1,3GT$ gene-inserted virus strain sequence. For this, the $\alpha1,3GT$-gene-carrying plasmid was amplified with GT-PF and GT-PR primers, and the target gene segment was obtained. LA3000-PF and LA3000-PR served as the primers to amplify and validate the successful synthesis of NDV-GT. Successful insertion of the $\alpha1,3GT$ gene in the NDV genome was assessed by sequencing.

Three helper plasmids, pCI-NP, pCI-P, and pCI-L, were co-transfected with the recombinant expression vector (NDV-GT) into BSR-T7/5 cells. After culturing for 60-72 h, cells were transferred to -80°C for three repeated freeze-thaw cycles. Subsequently, the cells and their supernatants were inoculated into 9-11 day-SPF chicken embryos at a dose of 0.2 mL/embryo, and the dead embryos were discarded within 24 h. The allantoic fluid was collected from the dead embryos after 24 h under aseptic conditions, and hemagglutination assay (HA) test was performed. The positive results in the HA test were considered to be indicative of the successfully rescued recombinant NDV-GT.

NDV-GT infection and $\alpha1,3GT$ gene expression in tumor cells

Tumor cell lines HepG2, HO8910, HeLa, A549, TE-10, SK-MEL-28, MDA-MB-231, and LS513, along with normal cells THLE-2, HUVEC, IMR-90, H9C2, HEK-293T, H9, and sperm were seeded at a density of 1.5×10^5/mL in 24-well plates containing coverslips. Additionally, ten ovum cells and ten blastula cells were added to each well in the 24-well plates. After 24 h, the medium was removed, and 1 mL of complete medium containing NDV-GT or NDV (0.1 MOI) was added. Control wells received 1 mL of complete medium. After 1 h infection, cells were washed with PBS and incubated in fresh medium. At 24 h, cells were fixed with 4% formaldehyde, incubated with NDV and αGal antibodies at 37°C for 1 h, washed with PBST, incubated with secondary antibodies at 37°C for 30 min in dark, and stained with DAPI before LCSM analysis for NDV infection and αGal immunofluorescence.

Immunofluorescence detection of complement deposition on tumor cells

HeLa cells were seeded in 24-well plates containing cell culture slides at a density of 1.5×10^5 cells/mL and incubated at 37°C for 24 hours. Subsequently, the culture medium was aspirated, and 1 mL of DMEM with 10% FBS containing diluted NDV or NDV-GT (0.1 MOI) was added to the respective wells. Control wells received 1 mL of DMEM with 10% FBS. One hour post-infection, cells were rinsed with fresh PBS and then incubated with DMEM supplemented with 5% human serum and 4.5×10^5 PBMCs. The αGal antibody blocking group was additionally supplied with 20 μL of αGal blocking antibody. After 24 hours, the medium was removed, and cells were fixed with 4% formaldehyde. They were then incubated with C3b and C4b antibodies at 37°C for 1 hour, followed by washing with PBST, incubated with secondary antibodies at 37°C for 30 min in dark, and stained with DAPI before LCSM analysis immunofluorescence expression of C3b and C4b.

Cell proliferation and apoptosis

HepG2, HO8910, HeLa, A549, and TE-10 cells in the logarithmic growth phase were treated with trypsin and suspended in complete medium at a density of 4×10^4/mL. A total of 100 μL of the cell suspension was added to each well of a 96-well plate and incubated at 37°C for 24 h. After incubation, the medium was removed, and 100 μL of diluted NDV or NDV-GT (0.1 MOI) complete medium were added to the wells of different groups, while 100 μL of complete medium was added to the control group. After 1 h of infection, cells were washed with PBS and incubated with 100 μL complete medium containing 5% human serum and 1.2×10^5/mL PBMCs. The αGal antibody blocking group was additionally supplied with 2 μL of αGal blocking antibody. After 24, 48, and 72 h of incubation, the medium was removed, and cells were washed with PBS. Ten μL of CCK-8 solution (5 mg/mL) were then added to each well and incubated for 4 h. Absorbance at 450 nm was measured using a microplate reader to calculate cell viability.

Flow cytometry for apoptosis detection

HepG2, HO8910, HeLa, A549, and TE-10 cells in the logarithmic growth phase were treated with trypsin and suspended in complete medium at a density of 4×10^4/mL. One mL of the cell suspension were then added to each well of a 12-well plate and incubated at 37°C for 24 h. After incubation, the medium was removed, and 1 mL of diluted NDV or NDV-GT (0.1 MOI) complete medium was added to the wells in different groups. The control group received 1 mL of complete medium. After 1 h infection, cells were washed with fresh PBS and incubated in 1 mL of complete medium containing 5% human serum and 1.2×10^5/mL PBMCs, the αGal antibody blocking group was additionally supplied with 20 μL of αGal blocking antibody, after 72 h, the medium was removed, and cells were digested with 0.25% trypsin without EDTA. The cells were collected, washed twice with PBS, and resuspended in 200 μL of binding buffer. Then, 10 μL of annexin V-FITC was added, and cells were incubated in the dark at 4°C for 10 min at room temperature. Finally, 200 μL of binding buffer and 5 μL of PI were added, mixed gently, and incubated in the dark at room temperature for 5 min before analysis by flow cytometry (Beckman).

Cynomolgus monkeys

Cynomolgus monkeys aged between 3.5 and 6 years were purchased from Changchun Biotechnology Co., Ltd. (Fangchenggang, Guangxi, China). The Experimental Animal Ethics Committee of Guangxi Medical University approved all animal maintenance and animal experiment procedures involved in this study (No.201901015). The cynomolgus monkey facility was notarized by the Association for Assessment and Accreditation of Laboratory Animal Care (AAALAC) International.

In vivo efficacy evaluation of NDV-GT in cynomolgus monkeys with CRISPR-mediated HCC

We used CRISPR/Cas9 technology to establish a primary HCC cynomolgus monkey model in our previous report.[46] This model enabled us to monitor tumor development using color-ultrasound imaging and confirm the presence of liver tumors via aspiration biopsy. To establish this model, the monkeys were anesthetized with intramuscular injection of Etamsylate (8.75 mg/kg). Subsequently, each monkey received weekly injections of Adeno-Pten-sgRNA (1×10^{11} PFU/kg), Adeno-p53-sgRNA (1×10^{11} PFU/kg), and Adeno-Cas9 (2×10^{11} PFU/kg) dissolved in 400 μL of normal saline (0.9% NaCl) into the left intrahepatic portal vein under ultrasonic guidance for 24 weeks. This comprehensive approach enabled us to study HCC development and treatment responses in this model, providing valuable insights for future HCC research and therapeutic development. Once the tumors reached approximately 1.0 cm in diameter, the monkeys were randomly assigned to three groups: (1) NDV-GT group ($n = 5$), where 1×10^7 PFU/kg of NDV-GT was administered intravenously weekly; (2) NDV group ($n = 5$), where 1×10^7 PFU/kg of NDV was injected intravenously weekly; and (3) PBS group ($n = 5$), where 1 mL of PBS was injected intravenously weekly for a total of 12 administrations. The tumor volumes in HCC-bearing monkeys were monitored weekly using the formula: $L \times W^2 \times 0.5$, where L and W, determined through ultrasound imaging, represent the length and width of the tumor, respectively. These measurements were conducted monthly to track tumor progression over time. Blood samples were collected to assess AFP levels before and after treatment. In addition, tumor tissues were surgically biopsied at 0, 24, 48, 72, and 96 hours, stained for immunofluorescence, and analyzed for NDV-GT distribution.

Hematoxylin-eosin (H&E) and immunofluorescence (IF) staining

At 24 hours after the twelfth week of treatment, tumor tissues and adjacent normal tissues were surgically biopsied from HCC-bearing monkeys for histological examination and IF staining. The HCC-bearing monkeys were anesthetized with 1% sodium pentobarbital (45 mg/kg) before surgical biopsy of tumor tissue. Tumor tissues were collected before and after NDV-GT treatment for histological analysis. Additionally, a minimally invasive laparoscopic biopsy of P2 (ovarian cancer) tumor tissue was performed before the initiation of NDV-GT and at the end of the third month of treatment. Briefly, for paraffin section preparation, tumor tissues were washed with PBS, fixed in paraformaldehyde, and embedded in paraffin; then, 5 μm sections were prepared for H&E and IF staining of CD31, CD105, and TUNEL, following the respective kit instructions. For frozen section preparation, tumor tissues were embedded in Optimal Cutting Temperature (OCT) compound, cryosectioned at 5 μm thickness using a cryostat, and subsequently blocked with bovine serum albumin (BSA), followed by IF staining for NDV, αGal, PAF, CD41, fibrinogen, granzyme B, perforin, CD4, CD8, C3b, and C4b, according to the manufacturer's kit protocols. All stained sections were analyzed using a Nikon confocal microscope (Japan). Additionally, all reagents used in this study were validated in our laboratory and confirmed to be suitable for this research.

Sequencing analysis

The tumor tissues from HCC-bearing monkeys in the different treatment groups were collected, and proteins were extracted for proteomic analysis using protein-chip technology. Sequencing and relative quantification of the proteins were performed to identify differentially expressed proteins. Subsequently, proteins were analyzed to investigate the molecular mechanism of NDV-GT oncolysis. The expression difference between the experimental and control groups for the up-regulated or down-regulated protein expression levels was set at 1.2 times or 0.83 times, respectively, for the difference to be considered as significant. The identified proteins were further validated using western blotting analysis.

The proteins with significant changes identified through proteomic analysis were further analyzed using the KEGG pathway database to explore their involvement in various signaling pathways. The original data were normalized using the software's built-in function. For differential protein analysis, a fold-change cut-off of ≤ 0.5 or ≥ 2 was applied, along with a fluorescence signal intensity threshold of > 500. Protein microarray analysis was performed to gain insights into the functional implications of the differentially expressed proteins. KEGG pathway enrichment analysis was utilized, and Fisher's exact test and the cluster profiler from R/Bioconductor were adopted for statistical evaluation. The selection criteria were set to include only those terms/pathways that had ≥ 5 differentially expressed genes, with a p value < 0.05. The enriched genes were ranked in descending order based on the count value, and the top 12 results were highlighted. The enrich factor was calculated to assess the significance of pathway enrichment. It was determined using the formula: enrich factor = $(N_1/N_{1\text{-total}})/(N_2/N_{2\text{-total}})$, where N_1 and $N_{1\text{-total}}$ represent the numbers of differentially expressed genes in some term and all differentially expressed genes, respectively, in the database; N_2 and $N_{2\text{-total}}$ represent the numbers of all genes in some term and all genes in the database, respectively. This analysis provided insights into the functional implications of the differentially expressed proteins and their potential roles in HCC development and treatment response.

Western blotting

HepG2 cells were seeded in 6-well plates and infected with the virus at 80% confluency. After infection for 1 h, the medium with PBMCs and 5% human serum and/or 5 μM Akt inhibitor (AKT-IN-6) was added, and HepG2 cells were incubated at 37°C. The cells were collected when 80%-90% of the cells were infected, then they were lysed, the SDS loading buffer was added and the sample boiled for 15 min, followed by SDS-PAGE electrophoresis and electro-transfer printing. After washing 3 times with PBS, cells were sealed with 5% skim milk overnight and further rinsed with PBST 3 times. The internal reference antibody (i.e., β-actin) was diluted with TBST at 1:1000, and anti-phospho-PI3K, anti-PI3K, anti-phospho-Akt, anti-Akt, anti-phospho-caspase-9, anti-caspase-9, anti-phospho-IKK, anti-IKK, anti-phospho-NF-κB, anti-NF-κB, anti-cleaved caspase-3, and anti-β-actin antibodies were diluted with PBS at a ratio of 1:1000. Subsequently, the blocking reagent was discarded, and the diluted antibodies were added and incubated overnight, followed by washing 3 times with PBST. Next, goat anti-rabbit IgG or goat anti-mouse IgG secondary antibody (1:1000) to rabbit was added and incubated for another 1 h, followed by washing 3 times with PBST. Finally, the samples were

scanned and analyzed using an Odyssey 3.0 system. The expressions of Akt, Casp9, IKK, NF-κB, and their phosphorylated forms, and cleaved caspase-3 in HepG2 cells treated with NDV-GT, NDV, or PBS were detected.

Enzyme-linked immunoassay for anti-αGal antibody

Three mL of peripheral blood were collected from cynomolgus monkeys and patients using dry blood collection tubes, and centrifuged at 2000 rpm for 10 min at 4 °C, and the upper serum was then removed to be measured. In light of the fact that murine adhesin can bind to anti-Gal, microplates were coated with 55 ng of murine adhesin, incubated for 24 h at 4 °C, and blocked with 1% BSA for 2 h at 37 °C. Fifty-five μL of serum samples were then added to each well and diluted with PBS containing 1% BSA with titers of variously 1:20, 1:40, 1:80, 1:160, 1:320, 1:640, 1:1280, and incubated at room temperature for 90 min, followed by washing 5 times with PBST. Fifty μL of rabbit anti-human IgG and IgM labeled with HRP were added and incubated at room temperature for 1 h. After washing the plates again, the absorbance values of each sample were recorded at 492 nm through optical density (OD) color rendering.

Enzyme-linked immunoassay for anti-NDV neutralizing antibody

Three mL of peripheral blood were collected from cynomolgus monkeys or patients using a dried blood collection tube, and then centrifuged at 2000 rpm and 4°C for 10 min and the upper serum samples obtained for testing. Fifty μL of standard products were added to an enzyme-labeled coated plate, and then 40 μL of sample dilution was added to the sample well. Subsequently, 10 μL of the sample solution were added and shaken gently. After sealing the plates with plate sealing film, they were incubated at 37°C for 30 min, and washed with 30 × distilled water. Afterwards, the sealing plate film was removed, the liquid was discarded, and then each well was filled with the washing liquid, stood for 30 seconds and then the washing liquid was discarded. This process was repeated five times with the final step being to pat the wells dry. Fifty μL of enzyme-conjugate reagent were then added to each well, followed by plate sealing with specific film and incubation at 37°C for 30 min. After that, the plate sealing film was removed and the liquid was discarded, and then the plate was shaken to dry. Subsequently, each well was filled with the washing liquid, stood for 30 seconds and then the washing liquid was discarded. This process was repeated five times with the final step being to pat each well dry. Finally, chromogenic agent A (50 μL) was added to each well, and then the chromogenic agent B (50 μL) was added, gently shaken and incubated at 37°C for 10 min in the darkness. Immediately afterwards, 50 μL of termination liquid were added to each well to terminate the reaction; finally, the OD value of each well was measured at 450 nm.

Safety evaluation in the preclinical study

Virus detection in tissues and organs

Our analysis focused on assessing the safety parameters in cynomolgus monkeys to gain insights into the toxicity resulting from the intravenous administration of NDV-GT. The objectives were to anticipate potential adverse reactions that may arise during clinical use of this oncolytic drug, evaluate any toxicity to specific organs or tissues resulting from repeated drug administration, and pinpoint key indicators for monitoring potential toxic responses in clinical trials. These safety indices are crucial for informing the development of appropriate safety protocols and treatment strategies for use in clinical trials.

Monitoring of general physiological indicators

During the *in vivo* experiments, monkeys underwent daily inspections, encompassing a comprehensive evaluation of various parameters. These assessments included the examination of their mental status, behavioral activities, feeding patterns, and drinking habits within the PBS control, NDV, and NDV-GT groups. Additionally, measurements of body weight, body temperature, and heart rate were taken once a week throughout the course of the study.

Hematology and coagulation tests

Blood samples were systematically collected from individuals in the PBS, NDV, and NDV-GT groups, beginning from the pre-injection phase and extending through to the final stages of injection. These samples were meticulously analyzed to monitor key hematological parameters, including white blood cells (WBC), red blood cells (RBC), and hemoglobin (Hb). Additionally, various other indices such as lymphocytes, platelet counts, neutrophils (NEU), prothrombin time (PT), activated partial prothrombin time (APTT), and fibrinogen (Fib) were also assessed. It is noteworthy that the fluctuations observed in these hematological indices did not exhibit any discernible correlation with the timing of drug administration. Moreover, all observed variations remained within the normal reference range, indicating the absence of any toxicological effects.

Liver function, kidney function, and blood glucose monitoring

During treatment, blood urea nitrogen (BUN), creatinine (CRE), aspartate aminotransferase (AST), alanine aminotransferase (ALT), and glucose (GLU) levels in each group were determined.

Urine and feces analysis

The blood, urine and feces samples and fecal occult blood samples of the cynomolgus monkeys were collected and analyzed during the treatment period.

Histopathological examination

To examine the effect of the oncolytic virus on the cynomolgus monkeys, the animals were euthanized 12 weeks after intravenous administration, and histopathological analysis was performed on important visceral organs from each treatment group.

QUANTIFICATION AND STATISTICAL ANALYSIS

Flow cytometry data analysis was conducted utilizing Kaluza 2.1 software, while WB data were scrutinized through the application of Odyssey 3.0. For the generation of illustrative figures, R scripting was employed. Analysis of LCSM images was facilitated by ImageJ 1.7.0. Basic statistical analyses and the production of graphical representations were executed using GraphPad Prism 8. Data were articulated as the mean value plus or minus the standard deviation (mean ± SD). Subsequent to the assessment of normality and variance homogeneity, a one-way ANOVA was executed, with pairwise comparisons being conducted via the LSD-t method. Statistical significances were categorized as follows: ns (not significant), $*p < 0.05$, $**p < 0.01$, $***p < 0.001$ and $****p < 0.0001$.

Supplemental figures

(legend on next page)

Figure S1. Sequencing and oncolytic efficiency of NDV-GT, related to Figure 1

(A) Schematic representation of NDV-GT engineering: the target gene (porcine α1,3GT) was integrated into the plasmid at the *Pme* I enzyme cutting site.

(B) The target gene (α1,3GT) segment (1,053 bp) in the expression plasmid was analyzed by gel electrophoresis following PCR amplification. M: marker; track 1: amplified α1,3GT segments.

(C) The expression of the target gene in NDV-GT was analyzed by reverse-transcription PCR (RT-PCR). M: marker; track 1: amplified α1,3GT segments.

(D) Sequencing of recombined NDV-GT.
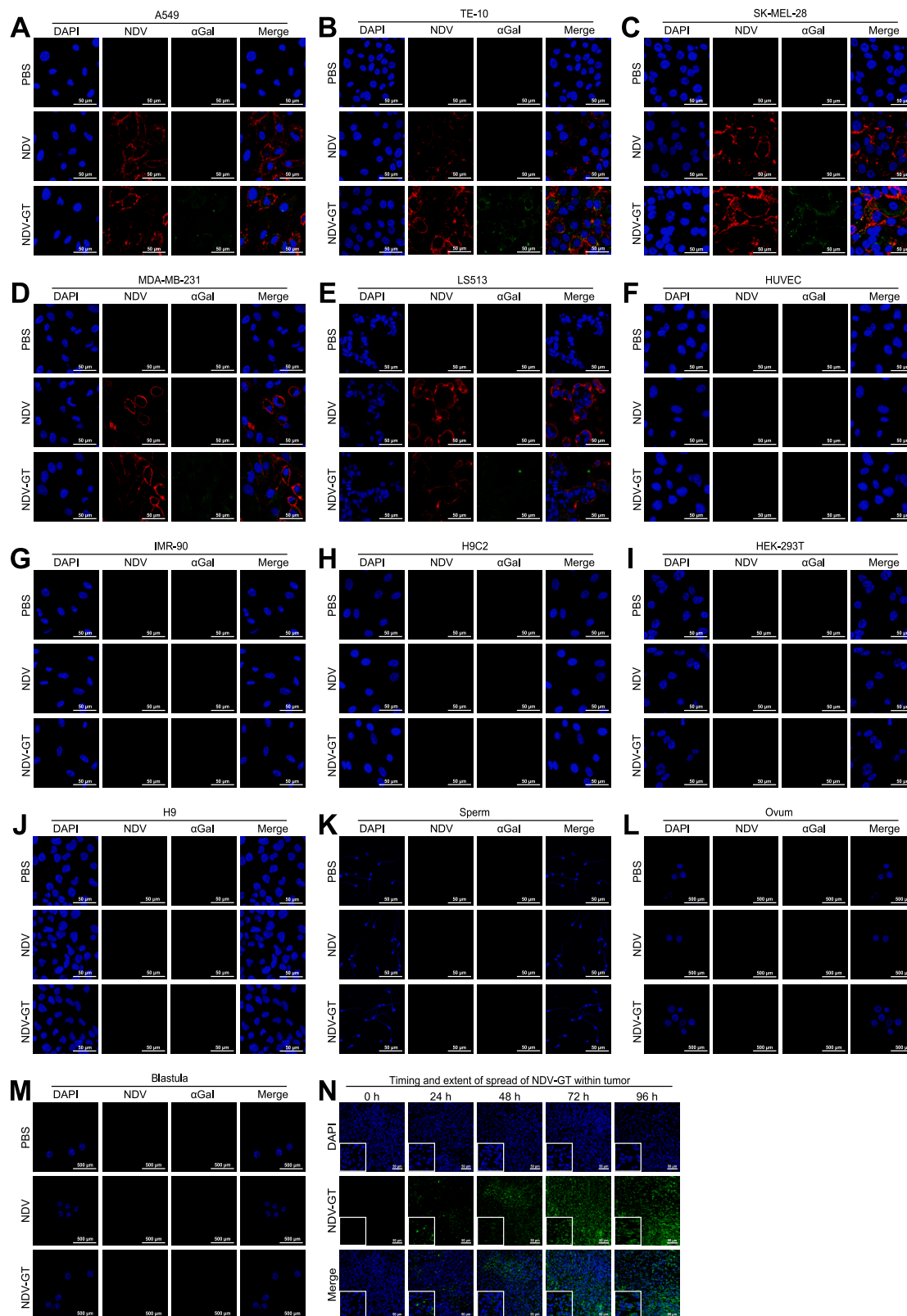
Figure S2. Specific targeting of NDV-GT to tumor cells, related to Figure 1

(A–M) Laser confocal scanning microscopy (LCSM) images of tumor and normal cell lines infected with NDV or NDV-GT. The images show tumor cell lines A549 (A), TE-10 (B), SK-MEL-28 (C), MDA-MB-231 (D), LS513 (E), and normal cells HUVEC (F), IMR-90 (G), H9C2 (H), HEK293T (I), H9 (J), sperm (K), ovum (L), and blastula (M) 1 h post-infection. Blue, red, and green fluorescences indicated the nuclei, NDV infection, and αGal expression, respectively. Red and green fluorescences in tumor cell lines (A–E) indicated NDV-GT infection and αGal expression, respectively, while the absence of red and green fluorescences in normal cells (F–M) suggested no infection. (A–K) Scale bar: 50 μm, magnification: 1,000×. (L and M) Scale bar: 500 μm, magnification: 100×.

(N) LCSM images revealed NDV-GT expression in tumors following intravenous injection. Tumor tissues were surgically biopsied at 0, 24, 48, 72, and 96 h, stained for immunofluorescence, and analyzed. Blue and green fluorescences indicated nuclei and NDV-GT, respectively. The number of cells with green fluorescence increased progressively, peaking at 72 h and remaining widespread at 96 h. Scale bars, 50 μm. 400× and 1,000× for the small box.
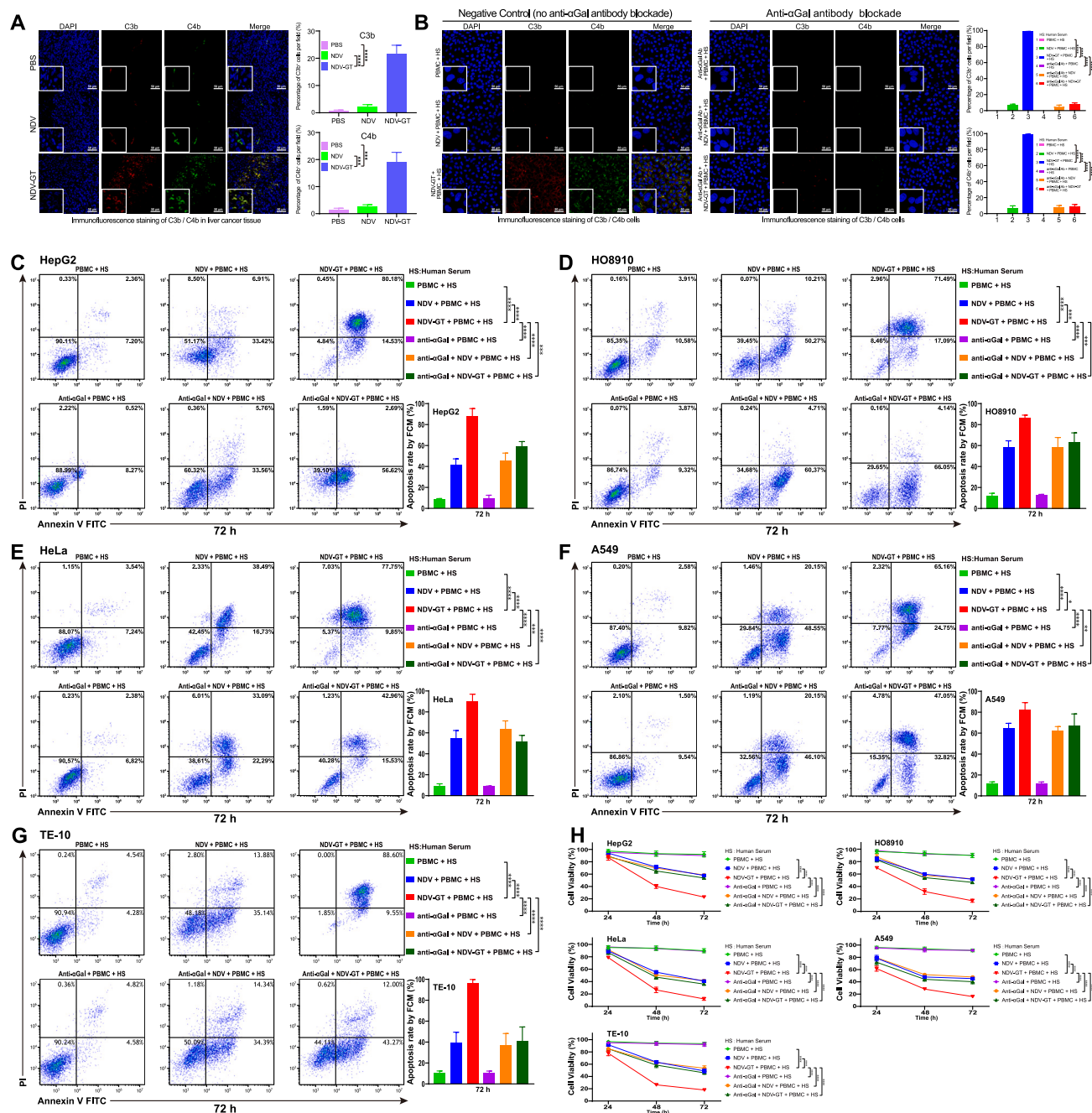
Figure S3. Antibody-dependent complement activation in NDV-GT-treated HCC, related to Figure 2

(A) Immunofluorescence images showing activated C3b and C4b deposition in tumor tissue. Compared with the NDV and PBS groups, significantly increased complement deposition was observed in the NDV-GT group. Data are presented as the mean ± SD (n = 3). ***p < 0.001, ****p < 0.0001. Scale bars, 50 μm. 400× and 1,000× for the small box.

(B) Immunofluorescence analysis of complement activation in NDV-GT via anti-αGal blocking. In the *in vitro* NDV-GT killing experiment simulating *in vivo* human conditions, we employed immunofluorescence to assess complement activation, revealing that anti-αGal blocking significantly reduced C3b and C4b deposition on tumor cells. Data are presented as the mean ± SD (n = 3). ****p < 0.0001. Scale bars, 50 μm. 400× and 1,000× for the small box.

(C–G) Apoptosis analysis of various human cancer cells post 72-h NDV-GT infection using flow cytometry. After 72-h co-incubation, flow cytometry analysis assessed apoptosis in HepG2 (C), HO8910 (D), HeLa (E), A549 (F), and TE-10 (G) cells co-incubated with PBMC + HS, NDV + PBMC + HS, NDV-GT + PBMC + HS,

(legend continued on next page)

anti-αGal + PBMC + HS, anti-αGal + NDV + PBMC + HS, and anti-αGal + NDV-GT + PBMC + HS. Data are expressed as mean ± SD ($n = 3$). *p < 0.05, **p < 0.01, ***p < 0.001, ****p < 0.0001. Results indicated a significant increase in cell apoptosis in the NDV-GT + PBMC + HS group compared with other groups at 72 h. (H) Cell viability of various cancer cells co-incubated with different treatments. Cell viability of HepG2, HO8910, HeLa, A549, and TE-10 cells co-incubated with PBMC + HS, NDV + PBMC + HS, NDV-GT + PBMC + HS, anti-αGal + PBMC + HS, anti-αGal + NDV + PBMC + HS, and anti-αGal + NDV-GT + PBMC + HS was assessed at 24, 48, and 72 h using CCK-8 assay. Data are presented as mean ± SD ($n = 8$). ****p < 0.0001. Results showed a marked decrease in cell viability in the NDV-GT + PBMC + HS group compared with other groups at 24, 48, and 72 h.
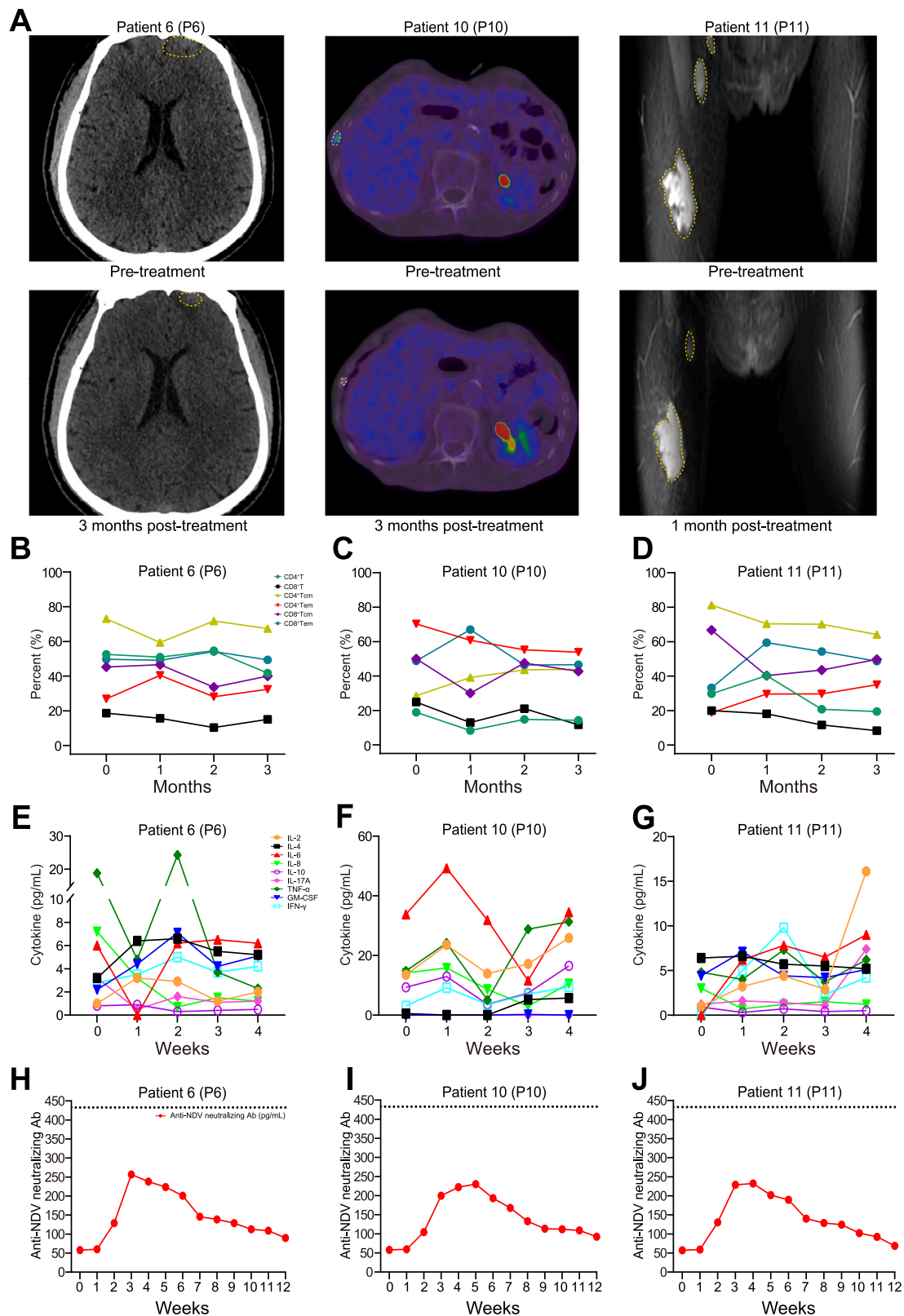
(legend on next page)

Figure S4. Clinical outcomes of NDV-GT therapy in patients with refractory lung cancer (P6), esophageal cancer (P10), and malignant melanoma (P11), related to Figure 4

(A) CT images of P6, a lung cancer patient with brain metastases pre- and post-intravenous NDV-GT treatment. After 3 months of treatment, the metastatic tumor in the left frontal lobe shrunk. The yellow dashed circles indicate the tumor lesions. PET-CT images of P10, an esophageal squamous cell carcinoma patient with bone metastasis pre- and post-intravenous combined with intraperitoneal injection of NDV-GT. After 3 months of treatment, metastatic tumor in the right rib was reduced, and the yellow dashed circles indicate the tumor lesions. MRI images of P11, a malignant melanoma patient with inguinal lymph node metastasis pre- and post-intravenous NDV-GT treatment. After 1 month of treatment, the tumor in the right leg was stable, and the lymph node with inguinal metastasis partially disappeared. The yellow dashed circles indicate the tumor lesions.

(B–D) FCM patterns for T cell subtypes.

(E–G) Levels of various cytokines, including IL-2, IL-4, IL-6, IL-8, IL-10, IL-17A, TNF-α, GM-CSF, and IFN-γ, were measured at different treatment periods (0, 1, 2, 3, and 4 weeks).
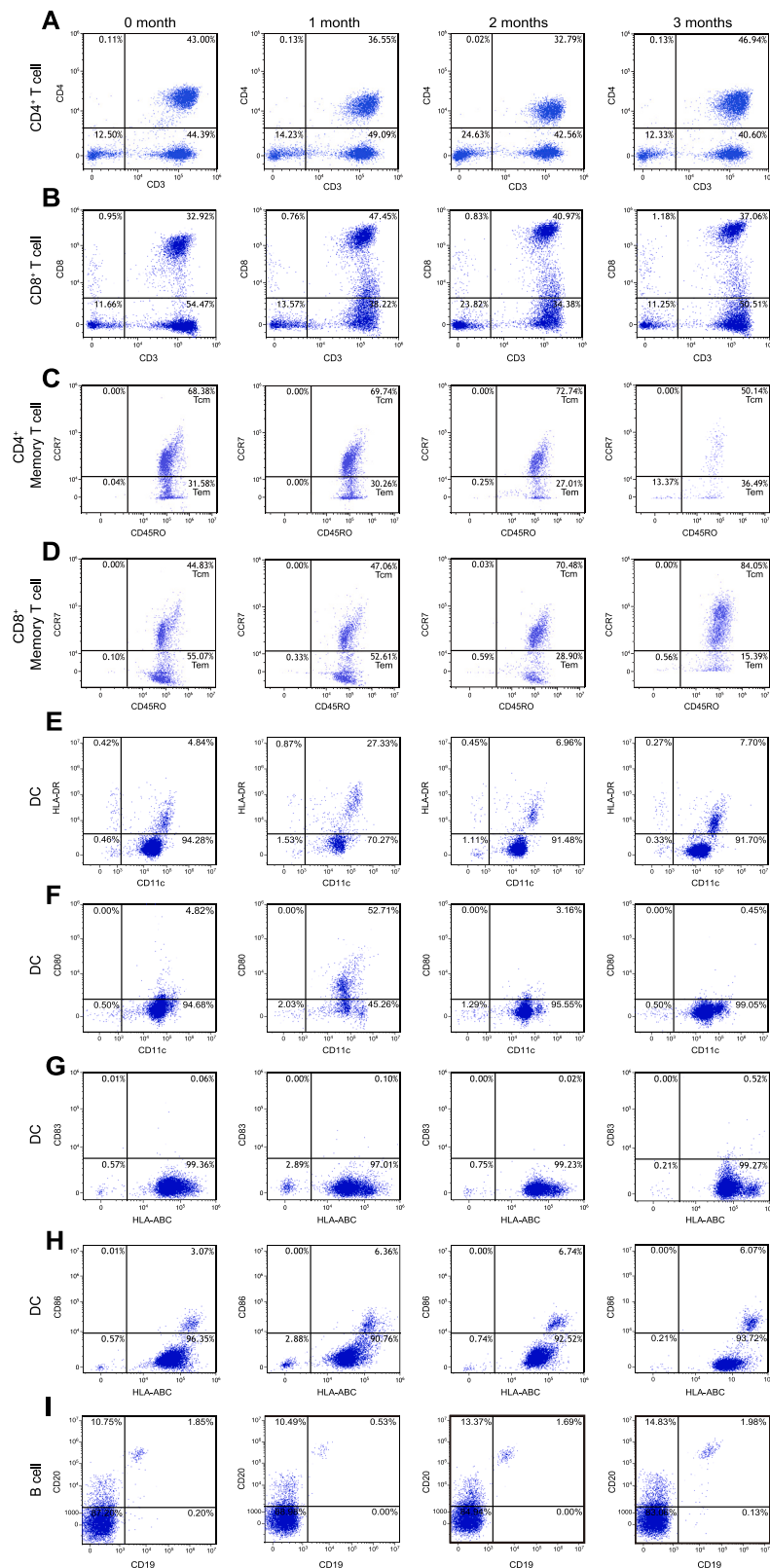
(H–J) Levels of anti-NDV neutralizing antibody were measured before and after treatment. No significant increase in the levels of this antibody was observed. The dashed lines indicate the upper limit of the normal control value range.
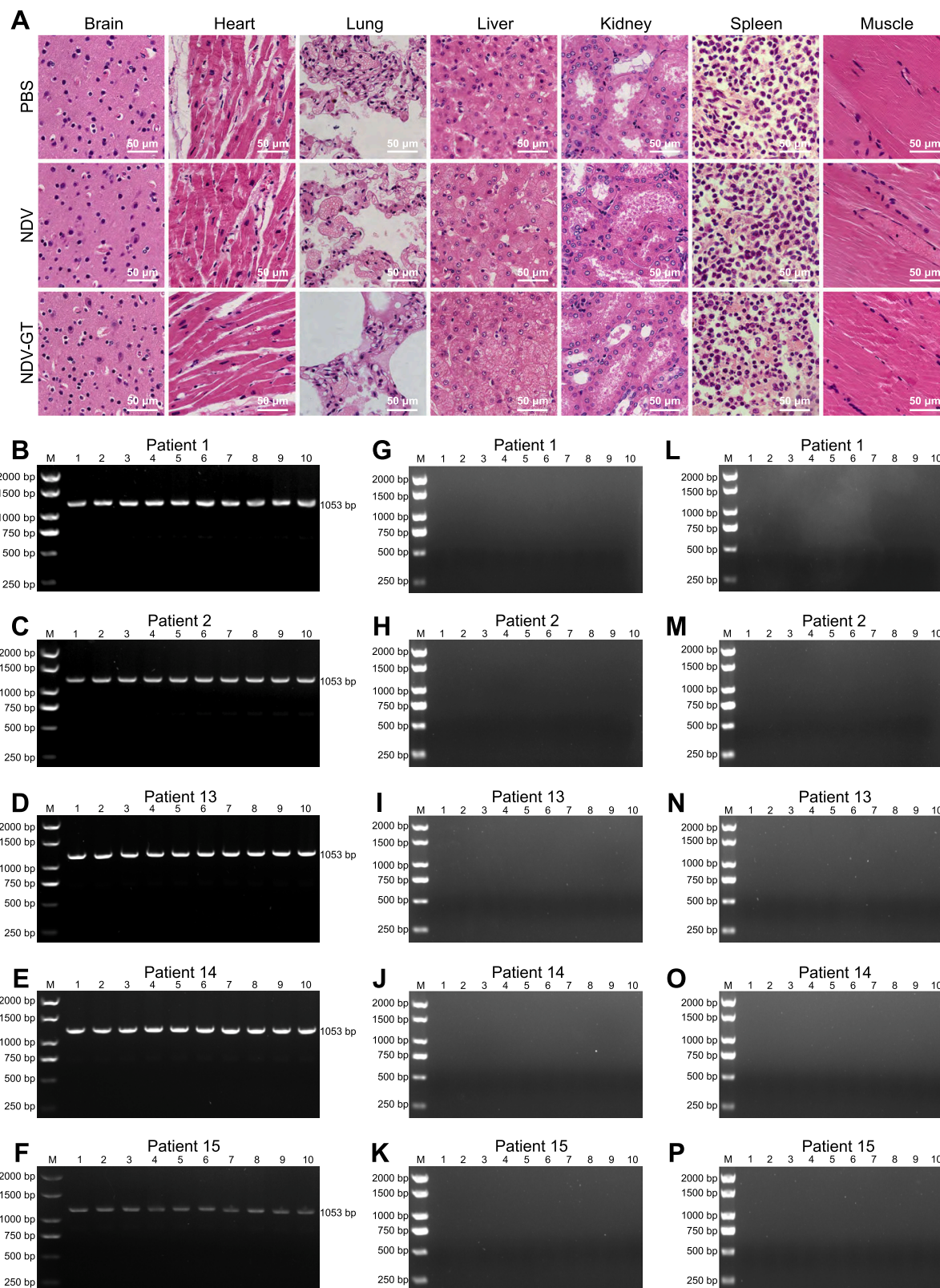
(legend on next page)

Figure S7. The safety evaluations of cynomolgus monkeys and the assessment of viral shedding from blood, stool, and urine of representative patients (P1, P2, and P13–P15), related to Figures 1, 2, 4, 5, 6, and 7

(A) Safety evaluation of H&E pathological examinations of main organs in cynomolgus monkeys treated with NDV-GT, NDV, and PBS. No adverse effects of the treatment were observed. Scale bars, 50 μm. 600× for the views.

(B–F) Expression of target gene $\alpha1,3GT$ of NDV-GT in serum samples of 5 patients during treatment every week. M: 2,000 bp marker; track 1–10: amplified $\alpha1,3GT$ segments in serum samples.

(G–K) Expression of target gene $\alpha1,3GT$ of NDV-GT in stools of 5 patients during treatment, M: 2,000 bp marker; track 1–10: amplified $\alpha1,3GT$ segments in stools.

(L–P) Expression of target gene $\alpha1,3GT$ of NDV-GT in urine of 5 patients during treatment, M: 2,000 bp marker; track 1–10: amplified $\alpha1,3GT$ segments in urine.